Composition and geochronology of the deep-seated xenoliths from the southeastern margin of the North China Craton.

UNIVERSITÀ DEGLI STUDI DI TORINO

Composition and geochronology of the deep-seated xenoliths in the southeastern margin of the North China Craton, and geological implications

Yi-Can Liu [a, *], An-Dong Wang [a], Shu-Guang Li [a], F. Rolfo [b, c], Yuan Li [a], C. Groppo [b], Xiao-Feng Gu [a], Zhen-Hui Hou [a]

[a] CAS Key Laboratory of Crust-Mantle Materials and Environments, School of Earth and Space Sciences, University of Science and Technology of China, Hefei 230026, China

[b] Department of Earth Sciences, University of Torino, Via Valperga Caluso 35, 1-10125 Torino, Italy

[c] C.N.R. – I.G.G., Section of Torino, Via Valperga Caluso 35, 1-10125 Torino, Italy

*Corresponding author. Tel./fax: +86 551 3600367.

E-mail address: liuyc@ustc.edu.cn (Yi-Can Liu)

ABSTRACT

In the southeastern margin of the North China Craton, a variety of deep-seated xenoliths, which have various mineral assemblages depending on their formation times, bulk compositions and metamorphic histories, occur with different sizes from 2 cm to 20 cm in diameter in Mesozoic dioritic porphyry. In this study, we present a combined petrologic, geochronological, Hf isotope and geochemical study on different types of xenoliths sampled from the same locality (Jiagou) and use these data to better constrain the composition and age of the deep crust beneath the area, thus shading new light on its late-Archean to Palaeoproterozoic crustal growth and evolution. Most of the xenoliths are mafic meta-igneous rocks, among which garnet-bearing lithologies are common. They can be classified into three broad petrographic groups: spinel-bearing garnet clinopyroxenite / phlogopite clinopyroxenite / spinel pyroxenite (Group 1), garnet amphibolite or hornblendite / garnet granulite / basic gneiss lacking pyroxene (Group 2), and garnet-bearing felsic (intermediate-acid) gneiss (Group 3). Generally, mafic-ultramafic rocks predominate whereas felsic rocks are rare. The protoliths of the studied xenoliths are igneous and range from basalt through andesite to dacite. Geochemical and Hf-isotope data indicate that most xenoliths for Groups 2 and 3 resemble those formed at a convergent continental margin arc setting, and a few (most of Group 1) represent mantle-derived products. Multiple metasomatic imprints have been recognized by multistage metamorphic mineral assemblages (e.g., different generations of amphibole) and ages. The occurrence of hydrous minerals such as multiple hornblendes and phlogopites in the xenoliths is the most important witness of a water-rich precursor and multistage metasomatism triggered by subduction-related or mantle-derived fluids or melts.

SHRIMP zircon U–Pb dating, Hf isotope and element geochemical data provide the solid evidence for the existence of subduction-related adakite-like and arc-related rocks in the southeastern margin of the North China Craton at ca. 2.5 Ga and 2.1 Ga, and confirm the occurrence of high-pressure granulite-facies metamorphism at ca. 1.8 Ga. These data suggest an episodic growth of Precambrian lower crust beneath the

region in response to two stages of subduction–accretion and one vertical accretion of mantle-derived basaltic magma at the base of the lower crust. Additionally, a previously unknown late mantle-derived basaltic magmatism at 393 ± 7 Ma has been recognized. Thus, the data presented in this paper demonstrate that the deep crust beneath the southeastern margin of the North China Craton is composed of a combination of different protoliths with a variety of Paleozoic, Palaeoproterozoic and late Neoarchaean sources, rather than rock types with a single origin as previously supposed, and is hybrid in composition. Therefore, the studied xenoliths have different origins, formed at different ages and originated at different levels of the deep crust.

Keywords: U-Pb dating; Hf isotope; lower crust; crustal growth; deep-seated xenoliths

1. Introduction

The formation of continental crust has been ascribed to two distinct plate tectonic settings: active continental margin and intra-plate (e.g., Rudnick, 1995). Growth of continents in within-plate settings occurs in response to plume-related magmatism, whereas the continental crust currently grows at the plate boundaries through magmatic additions and island arc collisions. Furthermore, convergent continental margins are well assessed to be a major site of lower crustal accretion through different mechanisms including basaltic underplating at the base of the crust and subduction–accretion (e.g., Weber et al., 2002, and references therein). However, relatively fewer examples of lower crustal xenoliths coming from active continental margins have been reported (e.g., Kempton et al., 1997; Weber et al., 2002). Crucial to all models of continental growth is knowledge of the petrology and geochemistry of the lower crust (Condie, 1997, 1999; Weber et al., 2002). However, our understanding of the Precambrian crust formation, especially lower continental crust, is generally hampered by the scarcity of data concerning deep crustal processes. At present, information on the lower continental crust is basically derived from studies on xenoliths in volcanic rocks, observations on exhumed granulite terrains and geophysical data, each one having its own advantages and limitations. Few, if any, exposed metamorphic terrains retain evidence of having formed near the base of the crust, and many have been modified by deformation and re-crystallization during uplift. Geophysical data are all remotely sensed and thus their interpretation without geological constraints can be speculative. As a consequence, xenoliths brought to the surface mainly by basaltic or dioritic volcanics were thought to provide direct windows into the present and/or fossil lower crust (e.g., Rudnick et al., 1986; Loock et al., 1990; Moser and Heaman, 1997; Upton et al., 2001; Weber et al., 2002; Zheng et al., 2003; Gao et al., 2004; Downes et al., 2007). In particular, mafic and ultramafic xenoliths are generally considered to represent current samples of inaccessible upper mantle and lower crustal lithologies (Montanini and Harlov, 2006).

Zircon retains a high-fidelity record of its crystallization history due to its

sluggish kinetic properties for U, Th and Pb (Cherniak and Watson, 2003) and is able to preserve multiple stages of magmatic and metamorphic records in high-grade metamorphic rocks involved in complex processes (e.g., Ayers et al., 2002; Möller et al., 2002; Hermann and Rubatto, 2003; Liu et al., 2011b), thereby readily amenable to be used for obtaining U–Pb ages in poly-metamorphic rocks (Liu et al., 2009, and references therein). Many studies have shown that U–Pb zircon geochronology is ideally suited for elucidating the temporal evolution of lower crustal xenoliths (e.g., Hanchar and Rudnick, 1995; Moser and Heaman, 1997). In addition, the Lu–Hf isotope system of zircon is generally more resistant to alteration processes than the U–Pb isotope system (Amelin et al., 2000; Cherniak and Watson, 2003; Zheng et al., 2006; Gerdes and Zeh, 2009). As a consequence, zircon preserves a high-quality record of near-initial Hf-isotope ratios, which can be used both in provenance studies and as a petrogenetic indicator (e.g., Griffin et al., 2004; Woodhead et al., 2004). The combined U–Pb and Lu–Hf isotope data for single zircon grains have been proven to provide reliable and very detailed information about the timing of magmatic and metamorphic events, as well as about the petrogenesis and the evolution of crust and mantle over time (e.g., Vervoort and Blichert-Toft, 1999; Amelin et al., 2000; Griffin et al., 2000, 2004; Andersen et al., 2002; Condie et al., 2005; Iizuka et al., 2005; Hawkesworth and Kemp, 2006; Wu et al., 2006; Zheng et al., 2006; Gerdes and Zeh, 2009; Kemp et al., 2009; Zeh et al., 2009).

The North China Craton (NCC) is one of the oldest cratons in the world and there are numerous U–Pb zircon geochronological data on its Precambrian metamorphosed basement or lower crust. The data show that except for minor >3.6 Ga components (Liu et al., 1992; Zheng et al., 2004a; Wu et al., 2008; Zhang et al., 2012), rocks of the NCC basement have U–Pb zircon ages clustering at 1.8–1.9 and ~2.5 Ga (e.g., Zhao et al., 2001; Gao et al., 2004; Zheng et al., 2004b; Santosh et al., 2007b; Liu et al., 2009, 2011a; Zhai and Santosh, 2011). The 2.5 Ga peak was considered to coincide with the major crustal growth period of the NCC (Gao et al., 2004). In addition, the basement rocks show a large range of Nd and Hf model ages with a peak at ~ 2.7 Ga, which is considered to be a major crustal growth period in the NCC (Jiang et al.,

2010). Based on Nd model ages, Wu et al. (2005) suggested that 2.8 Ga is the best estimate of the major mantle extraction age for the NCC and Zhai et al. (2005) considered that ca. 2.9–2.7 Ga is the main crust-forming episode in the NCC and that ~2.5 Ga age peak reflects a high-grade metamorphic event. Whether the most prominent ~2.5 Ga zircon age-peak or the ~2.8 Ga Nd model age-peak or ~2.7 Ga zircon Hf-model age-peak registers the major crustal growth period of the NCC is still uncertain.

However, in the southeastern margin of the NCC, there are numerous Mesozoic granitic or dioritic intrusions in the Xuzhou-Suzhou region and voluminous Mesozoic and Cenozoic volcanic rocks in the northeastern Anhui province and western Shandong Province which yield xenoliths of deep-seated rock types (Zhou et al., 1992; Xu et al., 1998, 2002, 2006, 2009; Zhang et al., 2002; Yu et al., 2003; Zheng et al., 2003, 2009; Huang et al., 2004; Zhang, 2005; Guo and Li, 2009; Liu et al., 2009). In this study, the target region is focused on the Xuzhou-Suzhou area and the object is the deep-seated xenoliths entrained in the Mesozoic Jiagou intrusion near Suzhou. Although the xenoliths in the studied area have previously been described and are considered to be formed at ~2.5 Ga and suffered from 1.8–1.9 Ga granulite-facies overprinting (Xu et al., 2002, 2006, 2009; Guo and Li, 2009; Liu et al., 2009), integrated petrographic, geochronological and geochemical studies on various xenoliths from the same locality are scarce. As a consequence, the composition and age of the deep crust beneath this portion of the NCC are not well-constrained; nevertheless, this information is essential for a robust understanding of the Precambrian crustal evolution and tectonic history of the area. Moreover, the nature and petrogenesis of the xenoliths also bear on the question as to whether or not they shared a common formational (~2.5 Ga arc origin) and evolutional history as proposed by Xu et al. (2009). In addition, so far, convincing evidence of a Paleozoic tectonothermal event has not been reported in the area except for the early Paleozoic (480 Ma) diamondiferous kimberlites from the intermediate segment of the Eastern Block of the NCC (Li et al., 2011 and references therein).

In this study, we present a combined petrologic, geochronological, Hf isotope and

geochemical study on different types of xenoliths from Jiagou in the southeastern margin of the NCC and use these data to better constrain the composition and age of the deep crust beneath the area, thus shading new light on its late Archean to Palaeoproterozoic crustal accretion and evolution. In particular, this study suggests a new interpretation of the composition, nature and age of the deep crust in the studied region, providing solid documentation for: (i) multiple crustal growth, (ii) its modification during the subsequent tectono-metamorphic events, and (iii) its interaction with the ascending mantle-derived magma. In addition, a Paleozoic mantle-derived magmatic event, leading to metasomatism on rocks of the deep crust beneath the region, has been recognized for the first time.

2. Geological setting

The NCC (Fig. 1) is one of the largest and oldest cratonic blocks in the world, as evidenced by the presence of > 3.6 Ga crustal remnants exposed at the surface or in lower crustal xenoliths (e.g., Liu et al., 1992; Zheng et al., 2004a; Wu et al., 2008; Zhang et al., 2012). The NCC underwent a series of tectonothermal events in late Archean and Palaeoproterozoic (e.g., Zhai et al., 2000; Zhai and Liu, 2003; Zhao et al., 2000, 2001; Wilde et al., 2002; Kusky and Li, 2003; Guo et al., 2005; Kröner et al., 2005; Hou et al., 2006, 2008; Tang et al., 2007; Guo and Li, 2009; Liu et al., 2009, 2011a; Jiang et al., 2010; Zhai and Santosh, 2011), and was stabilized in the late Palaeoproterozoic (e.g., Zhai et al., 2000) but experienced widespread tectonothermal reactivation during Mesozoic and Cenozoic (Zhou et al., 1992; Xu et al., 1998; Yu et al., 2003; Zheng et al., 2003, 2009; Huang et al., 2004; Xu et al., 2006; Liu et al., 2004, 2012; Zhang, 2012; Zhang et al., 2012). The NCC is bounded by faults and younger orogenic belts. The early Paleozoic Qilianshan orogen and the late Paleozoic Tianshan–Inner Mongolia–Daxinganling orogen bound the craton to the west and the north, respectively, whereas in the south the Mesozoic Qinling–Dabie–Sulu high- to ultrahigh-pressure (HP to UHP) belt separates the NCC from the Yangtze Craton. The NCC can be subdivided into the Eastern Block, the Western Block and the intervening

Trans-North China Orogen or Central Orogenic Zone (e.g., Zhao et al., 2000, 2001; Kusky and Li, 2003; Zhai and Liu, 2003; Kröner et al., 2005).

The Bengbu and Xuzhou–Suzhou areas lie in the Eastern Block along the southeastern margin of the NCC, about 100 km west of the Tan-Lu fault zone on the southwestern termination of the Sulu orogen and about 300 km north of the Dabie orogen and Hefei Basin (Fig. 1). The deformed Neoproterozoic to late Paleozoic sedimentary cover and late Archean to Palaeoproterozoic metamorphic basement in the region were intruded by several small Mesozoic intrusions (e.g. Jiagou, Banjing and Liguo) (Fig. 1) mainly composed of dioritic to monzodioritic porphyry. The Precambrian metamorphic basement in the studied area is mainly exposed at the surface in Bengbu, while no exposed basement occurs in the Xuzhou-Suzhou area where abundant deep-sourced enclaves occur in the Mesozoic intrusions (Xu et al., 2002, 2006, 2009; Guo and Li, 2009; Liu et al., 2009).

The studied samples were collected at the southeastern margin of the NCC from the xenoliths, which occur with different sizes from 2 cm to 20 cm in diameter in the Mesozoic dioritic porphyry at Jiagou near Suzhou (Figs. 1 and 2). While a lower crustal origin is evident for mafic garnet-bearing granulite or amphibolite and gneiss xenoliths (Huang et al., 2004; Liu et al., 2004, 2009), this is less evident for spinel-bearing garnet clinopyroxenite (see below). Moreover, it is not clear whether or not all the xenoliths of various lithologies share a common origin and formed in the same period. In order to better constrain the composition and age of the deep crust in this portion of the NCC, seventeen representative samples or xenoliths collected from the same locality at Jiagou were investigated through petrology and whole-rock geochemistry and five of them were also studied by *in situ* SHRIMP U-Pb dating, including two samples previously reported by Liu et al. (2009). At the same time, all the five dated xenoliths from Jiagou and a garnet amphibolite from the exposed Precambrian metamorphic basement in the Bengbu region dated by Liu et al. (2009) have been studied by means of zircon Hf-isotope analyses with the aim to better constrain the formation and evolution of lower crust in the region.

3. Petrography and samples

The xenoliths in the studied area are metamorphic rocks of deep-seated origin and comprise abundant mafic rocks, less common feldspar-free ultramafic types and rare felsic gneisses. No evidence was found of the eclogite xenoliths reported by Xu et al. (2002) in the same area. From a lithological viewpoint, the xenoliths include spinel-bearing garnet clinopyroxenite, phlogopite clinopyroxenite, spinel pyroxenite (websterite), garnet granulite, garnet amphibolite, garnet-bearing hornblendite and garnet-bearing mafic and felsic gneiss. Details of the petrography and mineral chemistry of the studied xenoliths were given in a separate paper (Liu et al., 2009) and are only summarized here. They can be classified into three broad petrographical groups: ultramafic spinel-bearing garnet clinopyroxenite / phlogopite clinopyroxenite / spinel pyroxenite (Group 1), mafic garnet amphibolite or hornblendite / garnet granulite / basic gneiss lacking pyroxene (Group 2) and felsic garnet-bearing gneiss (Group 3). Representative mineral compositions are reported in Table 1. Mineral abbreviations in figures and tables are after Whitney and Evans (2010).

Different mineral assemblages and compositions in the xenoliths reflect either different bulk-rock compositions or different metamorphic evolution. Group 1 includes spinel-bearing garnet clinopyroxenite and phlogopite clinopyroxenite (Fig. 3a–c). Spinel-bearing garnet clinopyroxenite is composed mainly of garnet, clinopyroxene and spinel with minor hornblende and biotite or phlogopite. Garnet occurs as exsolution lamellae in clinopyroxene, coronae around spinel and in the matrix. The occurrence of garnet exsolution is common in aluminous clinopyroxene from the mantle xenoliths of eclogite / garnet clinopyroxenite / pyroxenite found in kimberlite and alkali basalt (e.g., Sobolev and Sobolev, 1964; Lappin and Dawson, 1975). The development of this exsolution has been interpreted as the result of a slow isobaric cooling at upper mantle depths from high-temperature (e.g., Aoki et al., 1980; Sautter and Harte, 1988; Jerde et al., 1993). In addition, the occurrence of garnet coronae around spinel (Fig. 2a) suggests that Group 1 xenoliths formed under spinel-garnet–facies conditions. *P*–*T* conditions of spinel–garnet phase transition were

experimentally documented at 1.6–2 GPa and 900–1100 °C (e.g. O'Neill, 1981; Fan et al., 1997, and references therein). Therefore, such a spinel-bearing garnet clinopyroxenite was most likely of mantle origin.

In Group 2, the typical mineral assemblage is garnet, clinopyroxene, plagioclase, hornblende, quartz, ilmenite and rutile (Liu et al., 2009) (Fig. 3d, e). Interestingly enough, mafic granulites and garnet amphibolites or hornblendites coexist and have similar mineral assemblages and metamorphic evolution histories (Liu et al., 2009), most likely due to their different whole-rock compositions, local differences in fluid activity and various degrees of equilibration. Group 3 comprises plagioclase, hornblende, quartz, ilmenite and minor garnet and rutile (Fig. 3f). As a whole, Groups 2 and 3 xenoliths show a consistent peak metamorphic assemblage consisting of garnet, clinopyroxene, rutile, plagioclase, quartz, Ti-rich hornblende and Ti-rich biotite, indicative of HP granulite-facies metamorphism (Yardley, 1989; Pattison, 2003; O'Brien and Rötzler, 2003; Liu et al., 2009). Microstructural observations and mineral relationships suggest that this peak assemblage was followed by: (i) plagioclase + green hornblende + ilmenite + titanite; (ii) chlorite + calcite + magnetite. These assemblages are representative of amphibolite- and greenschist-facies metamorphic stages, respectively. Thermobarometric data and mineral assemblage suggested *P*–*T* conditions of 1.0–1.2 GPa and 800–860 °C for the HP granulite-facies metamorphic stage at *c.* 1.8 Ga (Liu et al., 2009).

All the xenoliths have undergone some retrogression promoted by hydration, with formation of mica (phlogopite and/or biotite), amphibole and chlorite but lacking any significant evidence of eclogite-facies overprint. The most abundant mineral is amphibole, followed by clinopyroxene and plagioclase. Garnet, rutile, plagioclase, ilmenite, quartz, apatite, spinel and corundum have also been identified; no olivine has been observed. The pervasive occurrence of amphibole and biotite or phlogopite implies a water-rich precursor and/or late modification by fluid and/or mantle metasomatism (see below). Furthermore, in Groups 2 and 3 xenoliths there are multiple generations of amphibole such as brown pargasite to ferro-pargasite and green magnesio-hastingsite or edenite as reported by Liu et al. (2009). Brown and

green hornblendes contain higher and lower amounts of TiO_2, respectively; they are inferred to have formed under different conditions, because it has been demonstrated that Ti increases with metamorphic grade (Raase, 1974; Pattison, 2003). This multiple stage of amphibole growth is also supported by textural evidence, with green hornblende occurring in retrograde symplectites or rimming the clinopyroxene margin and brown hornblende occurring as inclusions. It is thus evident that the xenoliths suffered multiple episodes of metamorphism and metasomatism.

K-feldspar is commonly associated with plagioclase or occurs along fractures within clinopyroxene (Fig. 3e) or garnet, suggesting a possible metasomatic origin due to solid-state infiltration of K-rich fluids/melts. These lines of evidence suggest that formation of K-feldspar in the mafic xenoliths reflects metasomatic processes, requiring an external K-rich fluid source, which operated in the lower crust during and after *in situ* high-T recrystallization of relatively dry rocks (Montanini and Harlov, 2006).

4. Analytical methods

4.1. *Whole-rock major and trace elements*

Whole-rock major element analysis was performed by wet chemical methods at the Langfang Laboratory, Hebei Bureau of Geology and Mineral Resources; trace element compositions were measured by an Elan DRCII ICP-MS at the CAS Key Laboratory of Crust-Mantle Materials and Environments, University of Science and Technology of China in Hefei. Analytical uncertainties range from ±1 to ±5% for major elements and ±5% to ±10% for trace elements. Detailed analytical procedures and instrument parameters for trace element analyses are reported in Hou and Wang (2007).

4.2. Zircon U-Pb dating

Zircons were separated from the whole-rock samples by crushing and sieving, followed by conventional magnetic and heavy-liquid separation and hand-picking

under binoculars. Approximately 200 zircon grains for samples 07JG32 and 07JG34 and 50 grains for sample 07JG30 were mounted using epoxy, together with a zircon U–Pb standard TEM (417 Ma) (Black et al., 2003). The mount was then polished until all zircon grains were approximately cut in half. The internal zoning patterns of the crystals were observed by cathodoluminescence (CL) imaging at Beijing SHRIMP Center, Chinese Academy of Geological Sciences (CAGS).

Zircons were dated on a SHRIMP II at Beijing SHRIMP Center. Uncertainties in ages are quoted at the 95% confidence level (2σ). A spot size of about 30μm was used. Common Pb corrections were made using measured ^{204}Pb. The SHRIMP analyses followed the procedures described by Williams (1998). Both optical photomicrographs and CL images were taken as a guide to select the U–Pb dating spots. Five scans through the mass stations were made for each age determination. Standards used were SL13, with an age of 572 Ma and U content of 238 ppm, and TEM, with an age of 417 Ma (Williams, 1998; Black et al., 2003). The U–Pb isotope data were treated following Compston et al. (1992) with the ISOPLOT program of Ludwig (2001). Measurement of standard zircon TEMORA 1 yielded a weighted ^{206}Pb/^{238}U age of 416.3 ± 3.2 Ma, which is in good agreement with the recommended isotope dilution-thermal ionization mass spectrometry (ID-TIMS) age of 416.75 ± 0.24 Ma (Black et al., 2003).

Mineral inclusions in zircon were identified using Raman spectroscopy at the Continental Dynamics Laboratory, CAGS and/or substantiated using the electron microprobe analyzer (EMPA) at the Institute of Mineral Resources, CAGS in China and at the Department of Mineralogical and Petrological Sciences, University of Torino in Italy. The analytical conditions on the Raman and EMPA were reported by Liu et al. (2009).

4.3. Zircon Lu-Hf isotope analysis

The laser ablation multi-collector inductively coupled plasma mass spectrometry (LA-MC-ICPMS) Lu–Hf isotope analysis was carried out at the Institute of Geology and Geophysics, the Chinese Academy of Sciences in Beijing. Instrumental conditions

and data acquisition followed those described by Xu et al. (2004) and Wu et al. (2006). A Geolas-193 laser-ablation microprobe was attached to a Neptune multi-collector ICPMS. Typical ablation times were 30 to 90 s with a 10 Hz repetition rate and laser power of 100 mJ/pulse, resulting in a beam depth of 30 to 50 μm. A stationary spot was used for core analyses with a beam diameter of about 63 μm. In contrast, a linear ablation was employed for rim and mantle analyses with a beam width of about 31.5 μm. Both He and Ar carrier gases were used to transport the ablated sample from the laser-ablation cell via a mixing chamber to the ICPMS torch. A signal collection model for one block with 200 cycles, in which one cycle has 0.131 s integration time and bulk time for one measurement lasts about 30 s. During analytical processes, the $^{176}Hf/^{177}Hf$ ratios of two standard zircons Mud Tank and GJ-1 were 0.282502 ± 5 and 0.282008 ± 7, respectively, which are in good agreement with the referenced $^{176}Hf/^{177}Hf$ ratios of 0.282507 ± 6 and 0.281999 ± 8 measured by using the solution method (Woodhead and Hergt, 2005; Wu et al., 2006). The main parameters used in the εHf(t) (t = crystallization time of zircon) and model age calculations are listed as follows: $(^{176}Lu/^{177}Hf)_{CHUR}$=0.0332 and $(^{176}Hf/^{177}Hf)_{CHUR,0}$=0.282772 for chondritic uniform reservoir (Blichert-Toft & Albarede, 1997), $(^{176}Lu/^{177}Hf)_{DM}$=0.0384 and $(^{176}Hf/^{177}Hf)_{DM}$=0.28325 for depleted mantle reservoir (Griffin et al., 2000). ^{176}Lu decay constant $\lambda = 1.865 \times 10^{-5}$ m.y was used for calculations (Soderlund et al., 2004).

5. Results

5.1. Whole-rock major and trace elements

Seventeen samples of xenoliths, representative of the three different groups mentioned above, have been analyzed in this study and show a broad range in major element composition (Table 2; Figs. 4 and 5). Based on the discriminant function (D.F.) proposed by Shaw (1972) and their high MgO contents, all the protoliths of the studied xenoliths are magmatic, in agreement with the igneous cores of their zircons in CL images (see below). The SiO_2 contents range between 37.92 and 67.06 wt.%,

spanning from mafic-ultramafic, minor intermediate and rare acid compositions with variable Mg-numbers (77–38) (Fig. 5). The studied xenoliths mostly derived from basaltic protoliths, ranging in composition from alkaline to subalkaline types, and a few from andesitic or dacitic protoliths (Fig. 4). The samples of the Group 1 may be basalts or basaltic rocks. For the Group 2, their protoliths are mostly basalts and basaltic andesites; among this group, samples 08JG08, 07JG34 and 07JG05-2 have higher Nb contents of 8.17-42.3 ppm (Table 2 and Fig. 5b), suggesting that their precursors were high-Nb (HNB) and Nb-enriched (NEB) basalts, respectively according to Sajona et al. (1996) and Martin et al. (2005). Among group 3, sample 07JG32 displays magnesian andesite characteristics with SiO_2 53.58 wt.% and MgO 5.48 wt.% (Calmus et al., 2003) whereas sample 08JG03 has the highest SiO_2 content (67.06 wt.%) and MgO 5.18 wt.%, suggestive of a dacite precursor (Fig. 4).

The REE patterns for the three types of xenoliths are also distinctive (Fig. 6). In Group 1, most samples have relatively flat REE patterns and a few show a weak LREE enrichment, generally associated with negative Eu anomalies. For Group 2, the samples display negative, positive or even no Eu anomalies and most of them show near-flat REE to slightly enriched LREE patterns, except for sample 07JG07 which exhibits a pronounced HREE enrichment which may be related to its higher modal amount of garnet. Within the investigated xenoliths, amphibole-rich ones (e.g., sample 07JG05-2) are more enriched in total REEs than the other xenoliths. In contrast, the two samples of Group 3 are characterized by the lack of Eu anomalies and by strongly fractionated LREE to HREE trends (Fig. 6).

Most of the Groups 2 and 3 xenoliths exhibit primitive-mantle-normalized negative Ta–Nb anomalies typical of an arc signature (Fig. 7b and c), this signature being also supported by Sr/Y–Y diagram in Fig. 8. Positive Ti anomalies, consistent with the occurrence of Fe–Ti oxides, are present in some of the Group 2 and mirrored by negative Ti anomalies in the Group 3 xenoliths.

Cr and Ni contents for the studied samples display a large variation between 4.5–448 ppm and 18.7–248 ppm, most probably resulted from their different origin or from the processes they suffered (e.g., metasomatism, see below); the highest values

(e.g. samples 07JG06, 07JG12 and 07JG21) are typical of primitive to slightly fractionated mantle-derived magmas (Embey-Isztin et al., 2003). This chance is also supported by the relatively high Mg-number of some samples, i.e. 54–77. In addition, the samples exhibit various Sr, Ba, Nb and Y contents, some of them having comparatively high ones (Table 2; Figs. 8 and 9).

5.2. SHRIMP zircon U–Pb dating

5.2.1. CL imaging and mineral inclusions in zircon

SHRIMP U-Pb dating, combined with CL information and mineral inclusions for the selection of specific locations in zircon, is one of the most powerful techniques to unravel complex histories of individual zircon grains occurring in multistage metamorphic rocks (e.g., Vavra et al., 1996; Gebauer et al., 1997; Hermann et al., 2001; Liu et al., 2009, 2011b). Although mineral inclusions in zircon, especially from lower crustal rocks or deep-seated xenoliths, are rare, they can be occasionally found and provide a direct link between zircon formation and metamorphism (e.g., Gebauer et al., 1997; Hermann et al., 2001; Liu et al., 2007, 2009, 2011b).

Sample 07JG30 (Group 1) contains rare zircon grains, most probably resulted from a mantle genesis. Except for three inherited zircons (Fig. 10c), others have similar CL images with typical oscillatory zoning, indicative of igneous origin (e.g., Hanchar and Rudnick, 1995; Gebauer et al., 1997). Some of them show a core-rim structure, but the rims are usually very thin (< 20 μm) and do not contain mineral inclusions (Fig. 10b).

On the basis of CL images and mineral inclusions, core-rim domains have been clearly recognized in zircon from samples 07JG34 (Group 2) and 07JG32 (Group 3) (Fig. 10d–p). Most of the zircons cores exhibit oscillatory growth zoning, which is typical of igneous origin. However, some cores are truncated, embayed or irregularly shaped (Fig. 10k, n), suggesting that they were partially or completely reabsorbed, probably in the presence of a fluid (e.g., Ayers et al., 2002). The rim domains contain garnet, clinopyroxene, plagioclase, quartz and rutile inclusions (Table 3; Fig. 10h, k, l, o, p), similar to those previously described by Liu et al. (2009), indicative of a typical

HP granulite-facies assemblage (e.g., O'Brien and Rötzler, 2003; Pattison, 2003).

5.2.2. U–Pb ages

Twelve U-Pb spot analyses were made on 11 zircon grains from sample 07JG30 (Group 1: Table 4 and Fig. 11a), including 3 inherited and 8 igneous zircon dots. Except for 2 grains, other 6 analyses of igneous zircons record $^{206}Pb/^{238}U$ concordant ages ranging from 384 to 410 Ma with a weighted mean age of 393 ± 7 Ma (MSWD = 0.83). This age is in good agreement with the age of 387 ± 13 Ma obtained from a metamorphic overgrowth rim of zircon previously dated from sample 07JG14 (Liu et al., 2009) within error, recording a thermal event induced by intrusion of concurrent mantle-derived magma.

Twenty-three U-Pb spot analyses were made on 22 zircon grains from sample 07JG34 (Group 2: Table 4 and Fig. 11b). 6 analyses of inherited zircons record $^{207}Pb/^{206}Pb$ concordant ages ranging from 2559 to 2696 Ma with a weighted mean age of 2631 ± 43 Ma (MSWD = 0.72). Except for spot 20.1, 8 analyses of igneous zircons record $^{207}Pb/^{206}Pb$ concordant ages ranging from 2389 to 2567 Ma with a weighted mean age of 2480 ± 49 Ma (MSWD = 0.59). 4 metamorphic rim domains of zircon record $^{207}Pb/^{206}Pb$ concordant ages ranging from 2147 to 2215 Ma with a weighted mean age of 2167 ± 58 Ma (MSWD = 0.14), consistent with the upper intercept age of 2165 ± 68 Ma defined by 6 spot analyses of rim domains within error. In addition, granulite-facies mineral inclusions such as garnet, clinopyroxene and plagioclase (Table 3; Fig. 10h, k) were found in metamorphic domains. In this regard, the age of 2167 ± 58 Ma records the timing of granulite-facies metamorphism whilst the 2480 ± 49 Ma age records the formation time of its igneous precursor.

Twenty U-Pb spot analyses were made on 20 zircon grains from sample 07JG32 (Group 3: Table 4; Fig. 11c). Two different textural populations of zircon can be easily discerned by means of integrated CL imaging, i.e. core and rim, each one recording discrete ages (Fig. 11c). The 5 analyses of the zircon core domains record $^{206}Pb/^{238}U$ concordant ages with a weighted mean age of 2121 ± 32 Ma (MSWD = 0.86) and 15 spot analyses of rim domains give a $^{206}Pb/^{238}U$ concordant age of 1805 ± 43 Ma. As

mentioned above, there are igneous zoning in the core domains (Fig. 10 m and n) and inclusions of garnet + rutile + quartz + plagioclase + clinopyroxene in the rim domains (Table 3; Fig. 10i, o and p) for zircon from the sample 07JG32. Therefore, these data suggest that the 2121 ± 32 Ma age represents its formation time whereas the 1805 ± 43 Ma age indicates the timing of the granulite-facies metamorphic stage.

In conclusion, zircons from the 3 dated xenolith samples, especially samples 07JG34 and 07JG32, exhibit clear core-rim patterns evidenced by CL images (and mineral inclusions). Samples 07JG30, 07JG34 and 07JG32 were formed at 393 ± 7 Ma, 2480 ± 49 Ma and 2121 ± 32 Ma, and the latter two samples experienced granulite-facies metamorphism at 2167 ± 58 Ma and 1805 ± 43 Ma, respectively. If combined with the reported sample 07JG14 from the same area, which recorded three metamorphic stages at 176 ± 2 Ma, 387 ± 13 Ma and 1811 ± 19 Ma (Liu et al., 2009), it is therefore consistent that the studied xenoliths derived from igneous precursors of various age (ca. 2.5 Ga, 2.1 Ga and 393 ± 7 Ma) which underwent variable degrees of metamorphic overprinting or reworking at ca. 2.1 Ga, 1.8 Ga, 393 ± 7 Ma and 176 ± 2 Ma respectively, these ages strongly depending on their formation time and derivation depths or crustal levels.

5.3. Zircon Lu–Hf isotope data

Some of the zircons analyzed for U–Pb were also analyzed for their Hf isotopic composition. As already mentioned, the Hf isotopic composition of zircons provides valuable and reliable information on the source and age of the magmatic protolith, and it is also a very useful way to discriminate between magmatic and inherited components. Ablation spots for the Hf analyses were sited at the same spots used for U-Pb dating analyses. The *in situ* Hf isotopic analyses of zircons from six samples are listed in Table 5 and shown in Figs. 12 and 13.

Zircon $\varepsilon_{Hf}(t)$ values (+ 0.5 to + 6.7) with T_{DM1} ages of 786 ± 40 Ma (MSWD = 0.47, n = 4), ranging from 754 to 1003 Ma for sample 07JG30 of Group 1 (Table 5 and Fig. 12a) are significantly indicative of mantle-derived components but probably contaminated by older crust because of the existence of inherited zircons (Fig. 10c).

The wide range of positive $\varepsilon_{Hf}(t)$ values (+1.0 to +12.1) for the samples of Group 2 suggests the derivation of the parental magmas of the zircons by a range of processes, including the melting of minor ancient crust and the addition of juvenile material. The Hf-isotope data for most zircons with ages 2.5–2.4 Ga indicate the early generation of juvenile crust, followed by reworking. However, the samples of Group 2 have older T_{DM2} ages, e.g. 2777 ± 31 Ma (MSWD = 2, n = 18) and 2720 ± 53 Ma (MSWD = 1.5, n = 4) for samples 07JG34 and 07JG12, respectively (Table 5 and Fig. 12b and c). In contrast, the sample 07JG32 of Group 3 have variable $\varepsilon_{Hf}(t)$ values of –5.1 to +3.8 with a weighted mean T_{DM2} age of 2518 ± 47 Ma (MSWD = 0.43, n = 7) (Table 5 and Fig. 12e).

In comparison, the sample 07FY01 from the exposed meta-basement at Bengbu displays high $\varepsilon_{Hf}(t)$ values of +8.1 to +10.3 and +1.3 to +3.5 at 2.1 and 1.8 Ga, respectively, with a Hf T_{DM2} age of 2137 ± 31 Ma (MSWD = 1.08, n = 8) (Table 5 and Fig. 12f). This Hf T_{DM2} age of 2137 ± 31 Ma probably shows its emplacement age while the timing of its HP granulite-facies metamorphic stage is 1839 ± 31 Ma (Liu et al., 2009).

6. Discussion

6.1. Composition and petrogenesis of the protoliths

The composition of the deep crust at the southeastern margin of the NCC can be constrained by investigations of chemical compositions, metamorphic evolution and isotope dating of the xenoliths. As mentioned above, most of the protoliths for the studied samples are basalt or basaltic andesite, and a few are magnesian andesite and dacite. Plagioclase-rich xenoliths (e.g., sample 07JG06) are characterized by pronounced positive Eu and Sr anomalies (Figs. 6 and 7) and relatively enriched LREE patterns, in addition to higher contents of Al_2O_3 and Ba (Table 2 and Fig. 9). Altogether, these features indicate that plagioclase accumulation played a significant role in the fractionation process and their protoliths were gabbros.

The precursors of Group 1 xenoliths are mainly composed of basalts or basaltic

rocks with extremely high Mg-number values (62–77), relatively low REE contents, high positive ε_{Hf} (t) values (+ 0.5 to + 6.7) and young formation time, strongly suggesting a mantle-derived magma origin at 393 ± 7 Ma. This is in agreement with the above petrographic observations such as garnet occurrence as coronae around spinel (Fig. 3a) and exsolution lamellae in clinopyroxene (Fig. 3b), suggestive of spinel-garnet–facies conditions. In addition, incompatible elements, such as high field strength elements (HFSE, e.g. Nb, Ta, Zr and Hf), are generally insensitive to fractional crystallization, secondary alteration and degrees of partial melting in the source region and thus can be used to evaluate the petrogenesis of the xenoliths. In the spider diagrams (Fig. 7a), some of the xenoliths show Nb depletion and Ba and Zr–Hf enrichment as the possible result of lower crustal contamination (e.g. Sun & McDonough, 1989), probably during their ascent; in fact, such contamination would produce negative Nb–Ta anomalies but positive Zr–Hf anomalies in a spider diagram.

Particularly distinctive for the xenoliths of Group 2 is the presence of large rutile grains and abundant garnet (Liu et al., 2009), similar in composition to the rutile-bearing garnet granulites from Lesotho (Rogers, 1977) and Kola (Kempton et al., 2001), most likely suggesting a similar petrogenesis. The protoliths of Group 2 xenoliths were basalt or basaltic andesite or gabbro (Figs. 4–6) and formed at ~2.5 Ga with subsequent granulite-facies metamorphic overprinting at ~2.1 and/or ~1.8 Ga, strongly depending on their crustal-levels or depths of provenance. Some samples have typically high Sr contents (>400 ppm) and Sr/Y ratios, suggestive of adakitic affinity (Defant and Drummond, 1990) (Table 2; Figs. 7 and 8). In view of the possible occurrence of an adakitic rock–basaltic andesite–Nb-enriched basalt association (Figs. 4–8), it is suggested that at least part of Group 2 xenolith's protoliths formed in a subduction-related arc setting which however probably involved a multistage process (e.g. Calmus et al., 2003; Wang et al., 2008; Manikyamba and Kerrich, 2011, and references therein). This interpretation is also supported in these samples, by multiple hydrous minerals such as Ti-rich and Ti-poor amphiboles, whereas the Ti-rich amphibole generally occurs as inclusions in garnet or plagioclase (Liu et al., 2009) indicative of hydrous precursors. However, the primitive

mantle-normalized spider diagrams (Fig. 7b) of garnet granulites and amphibolites from the Group 2 display variable geochemical characteristics, probably resulting from metamorphic overprinting and reworking of various intensity. Some samples have pronounced troughs at Nb–Ta, Th and Zr, and peaks at Zr and Sr which could be ascribed to the metasomatic enhancement of LIL elements in comparison to HFSE. Most samples of this type display flat REE patterns. However, samples 07JG05-2 and 07JG34 are light REE-enriched, while sample 07JG07 exhibits the enrichment of heavy REEs. Such variations of REE suggest a metasomatic overprint (see below).

Two samples of Group 3 have magnesian andesite and dacite protoliths with similar geochemical characteristics (Figs. 4 and 7c), characterized by high Sr contents and Sr/Y ratios typical of adakitic rocks (Table 2 and Fig. 8), providing evidence for a similar source and petrogenetic history. They display marked negative anomalies at Nb-Ta, P and Ti anomalies, and positive Ba anomalies, typical of an arc signature. In addition, the magnesian andesite is generally considered as deriving from the melting of arc mantle wedge peridotites having interacted with acidic melts originated from the subducted oceanic crust (e.g., Yogodzinski et al., 1995; Calmus et al., 2003). High Cr (204 ppm) and Ni (97.8 ppm) contents for sample 07JG32 of Group 3 xenoliths (Table 2) strongly support this scenario. In this context, the precursors for Group 3 most likely generated from the northward oceanic subduction beneath the southeastern margin of the NCC at ~2.1 Ga, giving way to metamorphic overprinting of the $\geq$ 2.5 Ga lower crustal rocks. Therefore, combined with Hf T_{DM2} ages with a peak at 2518 ± 47 Ma (MSWD = 0.43, n = 7) (Fig. 12d) and $\varepsilon_{Hf}(t)$ values of −5.1 to +0.3 (Table 5), the Group 3 xenoliths were probably derived from arc mantle wedge peridotites metasomatized by adakitic melts, and contaminated by ca. 2.5 Ga ancient crustal materials during their emplacement at ca. 2.1 Ga. In addition, similar to the Group 2, Group 3 xenoliths also recorded granulite-facies metamorphism at 1805 ± 43 Ma, originated from coeval large-scale mantle-derived magma activity as proposed by Liu et al. (2009).

In particular for the xenoliths of Groups 2 and 3, the predominance of garnet-rich mineral assemblages is consistent with a HP petrogenesis because of the thicker crust,

probably related to large igneous provinces which were documented to be connected to the presence of mantle plumes at ca. 1.8 Ga (Liu et al., 2009), especially if accompanied by rifting (e.g., White et al., 1987; Kempton et al., 2001). The higher temperatures associated with an ascending plume would also lead to more magnesian parental magmas, and the plume source would result in high Cr and Ni contents and Mg-number values, in agreement with the data presented in this study. Thus, most xenoliths of Groups 2 and 3, especially those with adakite-like Nb-enriched basalt and magnesian andesite precursors, contain significant contributions from slab melts, slab-derived fluids and the mantle wedge (Martin et al., 2005), involved in multistage metasomatism rather than a simple, single stage history.

However, although sample 07JG32 of Group 3 and sample 07FY01 from the metamorphosed basement formed at the same age of ~2.1 Ga, they have different ε_{Hf} (t) values of – 5.1 to + 0.3 and + 8.1 to + 10.3 (Table 5 and Fig. 13). We suggest that the latter sample probably represents a contemporaneous mantle-derived magmatism with the ~2.1 Ga subduction-related arc magmatism, but both of them subsequently experienced different evolutional processes (Fig. 13).

In summary, the above petrologic, geochronological and geochemical data have turned out to be complex with significantly different assemblages of mafic-ultramafic and intermediate-acid rocks in the deep crust beneath the region. It is difficult to relate these xenoliths to a single mantle source or petrogenetic process. However, it is clear that the xenoliths of Groups 2 and 3 are dominated by hornblende-bearing assemblages with hydrous precursors, similar to those formed at convergent continental margins such as the northern Andes (Weber et al., 2002). In addition, subduction generally brings large quantities of water and hydrous minerals deep into the mantle, resulting in a large volume of aqueous fluids in the mantle at continental convergent margins. As a consequence, the basaltic magma was rich in hydrous fluids and the consequently formed rocks contain a large quantity of hydrous minerals such as amphibole. Therefore, based on these lithologic associations in the xenoliths and their geochronological and geochemical characteristics, it is suggested that there were at least two stages of northward oceanic subduction beneath the region at ~2.5 and

~2.1 Ga, respectively. In this regard, at least before 2.1 Ga the southern margin of the North China Craton must have faced an open ocean, and should not have been connected to any other continental blocks. Moreover, the Group 1 xenoliths were resulted from a young mantle-sourced magmatism characterized by positive ε_{Hf} (t) values of + 0.5 to + 6.7 and extremely high Mg–number (62–77) values, giving rise to various degrees of enrichment in MgO, Cr and Ni (see below) on the Precambrian lower crust at about 390 Ma.

6.2. Precambrian episodic crustal growth

The compositional, geochronological and geochemical data of the xenoliths mentioned above suggest that both arc and plume components were present in the deep crust and the lower crust comprises chiefly subducted-related components, which can be related to the regional geology to produce a model of how and when the deep crust formed in the southeastern margin of the NCC.

The data on zircon U–Pb ages and Hf isotopes presented in this work clearly attest multistage thermal events during the crustal evolution in this region. At least three major groups of igneous zircons, suggesting different magma crystallization ages and interpreted as the formation time for the precursors of the xenoliths, can be evidently recognized. The first zircon population, recorded in the samples of Group 2, indicates that they formed at about 2.5 Ga, although the formation of the primordial lower crust of the region might have occurred even earlier, at ca. 2.7–2.8 Ga (e.g., Tang et al., 2007; Zheng et al., 2009; Jiang et al., 2010; Zhai and Santosh, 2011; Zhang, 2012; this study). The second zircon population from the Group 3 xenoliths defined ages of ca. 2.1 Ga and the third population gave ages of ca. 390 Ma. Combined with the petrographic and geochemical data provided in this paper, the former two ages represent the formation age of a subduction-related arc at a convergent continental margin and the latter age is related to a young mantle-sourced magmatism. Thus it is proposed that multiple crustal growth and subsequent metamorphic events, and interactions between the ascending mantle-derived magma and the lower crust result in high Cr and Ni contents for some xenoliths of Groups 2

and 3 (e.g., samples 07JG06, 07JG12 and 07JG32) (Table 2).

Moreover, as previously proposed by Liu et al. (2009), the ca. 1.8 Ga HP granulite-facies metamorphic event may be ascribed to large-scale crustal heating and thickening related to mantle-derived basaltic underplating at the base of the lower crust, as evidenced by widespread extension, rifting and related mafic magma emplacement in the NCC during this period, in response to a vertical accretion in the region. This metamorphic event can thus be considered to be plume-related, eventually contributing to the initiation of the break-up of the NCC from Columbia at ca. 1.8 Ga (Zhai and Santosh, 2011).

Therefore, the ages derived from zircon in the deep-seated xenoliths correlate well with the lower crustal history in this area, providing robust evidence of at least three major periods of crust formation attributed to subduction–accretion at ca. 2.5 Ga and 2.1 Ga, and magmatic underplating at ca. 1.8 Ga. The former event is consistent with the dominant age of the NCC Archean basement (e.g., Zhai et al., 2000; Zhao et al., 2000; Kusky and Li, 2003; Zhai and Liu, 2003; Gao et al., 2004; Guo et al., 2005; Kröner et al., 2005; Zhai et al., 2005; Hou et al., 2006; Liu et al., 2011a; Zhai and Santosh, 2011; Zhang, 2012). In view of predominant two-stage Hf model ages of 2777 ± 31 Ma and 2720 ± 53 Ma (Fig. 12a and b) and inherited zircon ages of 2631 ± 43 Ma (Fig. 11b), the 2.7 - 2.8 Ga event might represent an older crustal growth event in the area or in the whole of NCC as suggested by some researchers (Tang et al., 2007; Zheng et al., 2009; Jiang et al., 2010; Zhai and Santosh, 2011), but remains to be further constrained by more data. Consequently, different types of xenoliths suffered various degrees of metamorphic overprinting and modification, strongly depending on their precursor ages and derivation depths.

6.3. Multiple metasomatism and modification of the lower crust

Although metasomatism occurs commonly in mantle-derived ultramafic xenoliths (e.g., Hawkesworth et al., 1990; Kempton et al., 2001), there is little evidence for its widespread occurrence in the lower crust. Notable exceptions are the

amphibole-bearing Pl + Cpx ± Grt ± Opx granulites from the Eifel, Germany (Stosch and Lugmair, 1984) and amphibole-bearing Cpx + Grt + Pl ± Opx granulites from north Queensland (Stolz and Davis, 1989), as well as the Kola granulite xenoliths where phlogopite is the predominant hydrous phase (Kempton *et al.*, 2001). In contrast, K-rich (i.e. mica-rich) metasomatism of the lowermost crust–mantle boundary may be common for thick continental roots, although these are probably lost through delamination and recycling in tectonically active areas, and may only rarely be preserved (Kempton et al., 2001). However, the southeastern margin of the NCC experienced a complex crustal evolution involved in multistage tectonothermal events and related metamorphism, thus the deep-seated xenoliths in this area record petrographic and geochemical evidence for multiple metasomatic overprinting, resulting in variable degrees of modification. As an example, the pervasive occurrence of multiple amphiboles and biotites or phlogopites in various xenoliths, especially in Groups 2 and 3, implies a water-rich precursor and multistage fluid or melt or mantle metasomatism and widespread modification of the lower crust in this region.

Small amounts of Ti-rich biotite in textural equilibrium with a HP granulite-facies assemblage in the xenoliths of this region have been already reported (Liu et al., 2009). The Ti-rich biotite- and hornblende-bearing HP granulite-facies metamorphism have been documented to take place at about 1.8 Ga, with green hornblende and chlorite being originated from the late stages (see before). The green hornblende probably formed at 176 ± 2 Ma as defined by U-Pb dating of zircon overgrowth rim (Liu et al., 2009) and Ar-Ar dating of hornblende (Liu Y.-C. et al., unpublished data), whereas the chlorite was possibly produced by a more recent fluid-driven metasomatic event according to the petrographic observation. In this regard, the xenoliths suffered from at least three episodes of metasomatism: an older (late Palaeoproterozoic) one responsible for the growth of Ti-biotite and hornblende, and two younger (middle Jurassic to early Cretaceous) ones related to their exhumation and the related magmatism causing the growth of Ti-poor amphibole and the formation of chlorite. The former metamomatism was probably the result of the introduction of a fluid phase during HP metamorphism as suggested by Otten (1984).

Hydrous phase assemblages (e.g. green hornblende) partially replacing the granulite-facies minerals (e.g. clinopyroxene) (Fig. 3d and e) also suggest a fluid influx at amphibolite-facies conditions. An additional metasomatic event may be related to mantle-derived fluids or melts that resulted in the formation of phlogopite and metamorphic overprinting and modification on the rocks beneath the deep crust in this region, which produced MgO, Cr and Ni enrichments in some samples of Groups 2 and 3 during recent events such as 393 ± 7 Ma mantle-derived magmatism. Also, the LREE enrichment exhibited by some samples of Group 1 (sample 08JG09) and by amphibolites of Group 2 (samples 07JG05-2 and 07JG34) is more likely the result of local metasomatic modifications (Dessai et al., 2004), causing the formation of phlogopite and/or amphibole and the consequent enrinchment in LILE (e.g. Sr, Ba and K) and REE. The samples containing abundant amphiboles tend to be richer in REEs and show more LREE enrichments than the others (Fig. 6). Similar cases have been previously observed (e.g., Al-Mishwat and Nasir, 2004).

In addition, as mentioned above some xenoliths have been metasomatised by subduction-related fluid or melt, leading to varying degrees of Ba and Nb enrichments (Table 2 and Fig. 9) at a convergent continental margin setting. Furthermore, during the ascent/uplift process, some of the xenoliths might have been metasomatized by K-rich fluids or melts, probably derived from phlogopite breakdown at depth, leading to the development of K- and Rb-rich mica and K-feldspar (Fig. 3c and e) and large-ion lithophile (LILE) (Ba, Rb, K, and Sr) elemental enrichment (Table 2 and Fig. 7).

Therefore, multiple metasomatic episodes have been recognized in the xenoliths from the southeastern margin of the NCC. Moreover, many xenoliths of Groups 2 and 3 suffered from a variety of multiple mantle metasomatic processes during their evolution. However, more detailed geochronological and petrological studies will be required in order to define the precise features and timing of metasomatism in the area.

6.4. Possible eastern extension of the northern Qinling orogen beneath the

southeastern margin of the NCC

As mentioned above, a previously unknown late mantle-derived basaltic magmatic event at 393 ± 7 Ma has been recognized and resulted in metamorphic overprinting and modification on some rocks of the Precambrian lower crust at depth in the southeastern margin of the NCC. However, in the northern Qinling orogen, there is an extensive tectono-thermal event at about 400 Ma as reported by Mattauer et al. (1985), Li et al. (1989), Lerch et al. (1995), Xue et al. (1996), Hacker et al. (1998) and Zhai et al. (1998). Recently, Liu et al. (2006) also reported a SHRIMP U-Pb age of 386 ± 20 Ma dated on one metamorphic overgrowth rim in zircon from the garnet-bearing epidote-mica-quartz schist of 465 Ma with an arc affinity in the Beihuaiyang zone of the Dabie orogen. In this context, it seems plausible that the northern Qinling orogen continues to the eastern segment of the Dabie orogen and then beneath the southeastern margin of the NCC in the Suzhou region or even further to the East. This extension might be presently covered by the Neoproterozoic to late Paleozoic strata and by the Mesozoic basin sediments. Based on 786 ± 40 Ma Hf-model ages and positive $\varepsilon_{Hf}(t)$ values ranging mostly from + 3 to + 6 (Table 5 and Fig. 12) for magmatic zircons from 393 ± 7 Ma spinel-bearing garnet clinopyroxenite, it is inferred that there was a Neoproterozoic oceanic crust (now vanished) between the NCC and Yangtze Craton. This possibility, recently demonstrated by Peng et al. (2012) at the northern margin of the Yangtze Craton, however remains to be further investigated and constrained by more tight evidences.

7. Conclusions

The occurrence and characteristics of diverse xenoliths at Jiagou near Suzhou implies that the actual deep crustal structure and composition of the southeastern margin of the NCC may be the result of multiple magmatic activities and metamorphic processes. Based on integrated petrologic, geochronological, Hf isotope and geochemical data, a major result of our study is that different types of xenoliths in the region are firstly documented to be the end-products of multistage petrogenetic

processes involving several sources and protolith ages, as well as variable degrees of metamorphic overprinting and modification, strongly depending on the rock types and their evolutionary histories.

The deep-seated xenoliths from the Mesozoic Jiagou dioritic porphyry in the southeastern margin of the NCC comprise a suit of mostly mafic rock types such as garnet amphibolite, garnet granulite, spinel-bearing garnet clinopyroxenite, garnet-bearing mafic gneiss and spinel pyroxenite (websterite) with minor garnet-bearing hornblendite and felsic gneiss, some of which are characterized by HP granulite-facies metamorphism, probably reflecting major crustal thickening and representing the lowermost part of lower crust. Whole-rock major, trace element and rare earth element characteristics show that the xenoliths include ultra-mafic, mafic and intermediate-acid groups. Most of the protoliths are alkaline and subalkaline basalt, while a few are gabbro, basaltic or magnesian andesite and dacite. Some of the xenoliths probably had the same mantle source but experienced different modification by late events (e.g., metasomatism), and formed at the base of the lower continental crust by mantle-derived magma underplating.

Geochronological and geochemical features of different types of xenoliths testify the significant compositional complexity of the deep crust in the southeastern margin of the NCC. SHRIMP zircon U–Pb dating and geochemical data of the xenoliths presented in this study, combined with their tectonic setting, provide the solid evidence for the existence of subduction-related adakite-like and arc-related rocks in the southeastern margin of the NCC at ca. 2.5 Ga and 2.1 Ga. Our data further confirm the occurrence of HP granulite-facies metamorphism at ca. 1.8 Ga, involved in a multistage process of continental growth in response to two stages of subduction–accretion and one vertical accretion of basaltic magma at the base of the lower crust, respectively. The 2.7 to 2.8 Ga ages defined by inherited zircons and depleted mantle zircon-Hf model ages could record an earlier crustal growth episode in the area.

The compositional and age variability shown by the xenoliths suggests that their igneous protoliths are the products of several episodes of subduction or magmatic

underplating and tectonic activity, though most samples of Groups 2 and 3, excluding Group 1, shared a common metamorphic evolution after 1.8 Ga. Therefore, the studied xenoliths have different origins, formed at different ages and originated at different levels of the deep crust, and thus are unlikely to share a common formational and evolutionary history as previously claimed.

Furthermore, on the base of these data the northern Qinling orogen most likely extends into the southeastern margin of the NCC and is covered by the Neoproterozoic to late Paleozoic strata and by the Mesozoic basin sediments widespread in the region.

Acknowledgements

This study was financially supported by the National Natural Science Foundation of China (Grant Nos. 90814008, 40634023 and 40973043) and the National Basic Research Program of China (Grant No. 2009CB825002). Laboratory work in Torino was supported by the Project "Scambi Culturali" (ROFRSCUL06 and ROFRSC07). We thank D.-Y. Liu, B. Song and H.-Q. Xie for their help in SHRIMP U-Pb dating, J.-H. Yang and Y.-H. Yang for Hf-isotope and trace-element analysis on zircon, L. Yan for Raman analysis and Z.-Y. Chen for electron microprobe analysis. Jörg Hermann and Tsuyoshi Iizuka are thanked for their suggestions and discussion on an earlier version of this manuscript, which helped clarify some ambiguities as well as the English presentation. Many suggestions and constructive comments by M. Santosh and two anonymous reviewers have greatly improved the paper.

References

Al-Mishwat, A. T., Nasir, S. J., 2004. Composition of the lower crust of the Arabian Plate: a xenolith perspective. Lithos 72, 45–72.

Amelin, Y., Lee, D.-C., Halliday, A. N., 2000. Early–middle Archean crustal evolution deduced from Lu-Hf and U-Pb isotopic studies of single zircon grains. Geochimica et Cosmochimica Acta 64, 4205–4225.

Andersen, T., Griffin,W. L., Pearson, N. J., 2002. Crustal evolution in the SW part of the Baltic Shield: the Hf isotope evidence. Journal of Petrology 43, 1725–1747.

Aoki, K. I., Fujimaki, H., Kitamura, M., 1980. Exsolved garnet-bearing megacrysts from some South African kimberlites. Lithos 13, 269–279.

Ayers, J. C., Dunkle, S., Gao, S., Miller, C. F., 2002. Constraints on timing of peak and retrograde metamorphism in the Dabie Shan ultrahigh-pressure metamorphic belt, east–central China, using U–Th–Pb dating of zircon and monazite. Chemical Geology 186, 315–331.

Blichert-Toft, J., Albarede, F., 1997. The Lu-Hf isotope geochemistry of chondrites and the evolution of the mantle-crust. Earth and Planetary Science Letters 148, 243–258.

Black, L. P., Kamo, S. L., Allen, C. M., Aleinikoff, J. K., Davis, D. W., Korsch, R. J., Foudoulis, C., 2003. TEMORA 1: A new zircon standard for Phanerozoic U-Pb geochronology. Chemical Geology 200, 155–170.

Calmus, T., Aguillón-Robles, A., Maury, R. C., Bellonb, H., Benoitd, M., Cotten, J., Bourgois, J., Michaud, F., 2003. Spatial and temporal evolution of basalts and magnesian andesites (‘‘bajaites’’) from Baja California, Mexico: the role of slab melts. Lithos 66, 77–105.

Cherniak, D. J., Watson, E. B., 2003. Diffusion in zircon. Reviews in Mineralogy and Geochemistry 53, 113–143.

Compston, W., Williams, I. S., Kirschvink, J. L., Zhang, Z., Ma, G., 1992. Zircon U-Pb ages for the Early Cambrian time-scale. Journal of the Geological Society, London 149, 171–184.

Condie, K. C., 1997. Contrasting sources for upper and lower continental crust: The

greenstone connection. The Journal of Geology 105, 729–736.

Condie, K. C., 1999. Mafic crustal xenoliths and the origin of the lower continental crust. Lithos 46, 95–101.

Condie, K. C., Beyer, E., Belousova, E., Griffin,W. L., O'Reilly, S. Y., 2005. U-Pb isotopic ages and Hf isotopic composition of single zircons: The search for juvenile Precambrian continental crust. Precambrian Research 139, 42–100.

Defant, M. J., Drummond, M. S., 1990. Derivation of some modern arc magmas by melting of young subducted lithosphere. Nature 347, 662–665.

Dessai, A. G., Markwick, A., Vaselli, O., Downes, H., 2004. Granulite and pyroxenite xenoliths from the Deccan Trap: insight into the nature and composition of the lower lithosphere beneath cratonic India. Lithos 78, 263–290.

Downes, H., Upton, B. G. J., Connolly, J., Beard, A. D., Bodinier, J. L., 2007. Petrology and geochemistry of a cumulate xenolith suite from Bute: evidence for late Palaeozoic crustal underplating beneath SW Scotland. Journal of the Geological Society, London 164, 1217–1231.

Embey-Isztin, A., Downes, H., Kempton, P. D., Dobosi, G., Thirlwall, M., 2003. Lower crustal granulite xenoliths from the Pannonian Basin, Hungary. Part 1: mineral chemistry, thermobarometry and petrology. Contributions to Mineralogy and Petrology 144, 652–670.

Fan, Q., Liu, R., Xie, H., Zhang, Y., Xu, P., Lin, Z., 1997. Experimental study of spinel-garnet phase transition in upper mantle and its significance. Science in China (Series D) 40, 383–389.

Gebauer, D., Schertl, H.-P., Brix, M., Schreyer, W., 1997. 35 Ma old ultrahigh-pressure metamorphism and evidence for very rapid exhumation in the Dora Maira Massif, Western Alps. Lithos 41, 5–24.

Gao, S., Rudnick, R.L., Yuan, H., Liu, X., Liu, Y., Xu, W., Ling, W., Ayers, J., Wang, X., Wang, Q., 2004. Recycling lower continental crust in the North China craton. Nature 432, 892–897.

Gerdes, A., Zeh, A., 2009. Zircon formation versus zircon alteration – New insights from combined U-Pb and Lu-Hf in-situ LA-ICP-MS analyses, and consequences

for the interpretation of Archean zircon from the Central Zone of the Limpopo Belt. Chemical Geology 261, 230–243.

Griffin, W. L., Pearson, N. J., Belousova, E., Jackson, S. E., van Achterbergh, E., O'Reilly, S. Y., Shee, S. R., 2000. The Hf isotope composition of cratonic mantle: LA-MC-ICPMS analysis of zircon megacrysts in kimberlites. Geochimica et Cosmochimica Acta 64, 133–147.

Griffin, W. L., Belousova, E. A., Shee, S. R., Pearson, N. J., O'Reilly, S. Y., 2004. Archean crustal evolution in the northern Yilgarn Craton: U-Pb and Hf-isotope evidence from detrital zircons. Precambrian Research 131, 231–282.

Guo, S., Li, S., 2009. SHRIMP zircon U-Pb ages for the Palaeoproterozoic metamorphic-magmatic events in the southeast margin of the North China Craton. Science in China (Series D) 52, 1039–1045.

Guo, J. H., Sun, M., Chen, F. K., Zhai, M. G., 2005. Sm–Nd and SHRIMP U–Pb zircon geochronology of high-pressure granulites in the Sanggan area, North China Craton: timing of Paleoproterozoic continental collision. Journal of Asian Earth Sciences 24, 629–642.

Hanchar, J. M., Rudnick, R. L., 1995. Revealing hidden structures: the application of cathodoluminescence and back-scattered electron imaging to dating zircons from lower crustal xenoliths. Lithos 36, 289–303.

Hacker, B.R., Ratschbacher, L., Webb, L., Ireland, T., Walker, D., Dong, S., 1998. U/Ph zircon ages constrain the architecture of the ultrahigh-pressure Qinling-Dabie Grogen, China. Earth and Planetary Science Letters 161,215–230.

Hawkesworth, C.J., Erlank, A.J., Kempton, P.D., Waters, F.G., 1990. Mantle metasomatism: isotope and trace-element trends in xenoliths from Kimberley, South Africa. Chemical Geology 85, 19–34.

Hawkesworth, C. J.. Kemp, A. I. S., 2006. Using hafnium and oxygen isotopes in zircons to unravel the record of crustal evolution. Chemical Geology 226, 144–162.

Hermann, J., Rubatto, D., Korsakov, A., Shatsky, V.S., 2001. Multiple zircon growth during fast exhumation of diamondiferous, deeply subducted continental crust

(Kokchetav massif, Kazakhstan). Contributions to Mineralogy and Petrology 141, 66–82.

Hermann, J., Rubatto, D., 2003. Relating zircon and monazite domains to garnet growth zones: age and duration of granulite facies metamorphism in the Val Malenco lower crust. Journal of Metamorphic Geology 21, 833–852.

Hou, G., Liu, Y., Li, J., 2006. Evidence for ~1.8 Ga extension of the Eastern Block of the North China Craton from SHRIMP U–Pb dating of mafic dyke swarms in Shandong Province. Journal of Asian Earth Sciences 27, 392–401.

Hou, Z., Wang, C., 2007. Determination of 35 trace elements in geological samples by inductively coupled plasma mass spectrometry. Journal of University of Science and Technology of China 37, 940–944 (in Chinese with English abstract).

Hou, G., Li, J., Yang, M., Yao, W., Wang, C., Wang, Y., 2008. Geochemical constraints on the tectonic environment of the Late Palaeoproterozoic mafic dyke swarms in the North China Craton. Gondwana Research 13, 103–116.

Huang, X.L., Xu, Y.G., Liu, D.Y., 2004. Geochronology, petrology and geochemistry of the granulite xenoliths from Nushan, east China: implication for a heterogeneous lower crust beneath the Sino-Korean Craton. Geochimica et Cosmochimica Acta 68, 127–149.

Iizuka, T., Hirata, T., Komiya, T., Rino, S., Katayama, I., Motoki, A., Maruyama, S., 2005. U–Pb and Lu–Hf isotope systematics of zircons from the Mississippi River sand: implications for reworking and growth of continental crust. Geology 33, 485–488.

Jerde, E. A., Taylor, L. A., Crozaz, G., Sobolev, N. V., 1993. Exsolution of garnet within clinopyroxenes of mantle eclogites: major- and trace-element chemistry. Contributions to Mineralogy and Petrology 114, 148–159.

Jiang, N., Guo, J., Zhai, M., Zhang, S., 2010. ~2.7 Ga crust growth in the North China craton. Precambrian Research 179, 37–49.

Kemp, A. I. S., Foster, G. L., Schersten, A., Whitehouse, M. J., Darling, J., Storey, C., 2009. Concurrent Pb-Hf isotope analysis of zircon by laser ablation

multi-collector ICP-MS, with implications for the crustal evolution of Greenland and the Himalayas. Chemical Geology 261, 244–260.

Kempton, P. D., Downes, H., Embey-Isztin, A., 1997. Mafic granulite xenoliths in Neogene alkali basalts from the western Pannonian basin: insight into the lower crust of a collapsed orogen. Journal of Petrology 38, 941–970.

Kempton, P. D., Downes, H., Neymark, L. A., Wartho, J. A., Zartman, R. E., Sharkov, E. V., 2001. Garnet granulite xenoliths from the northern Baltic Shield—the underplated lower crust of a Palaeoproterozoic large igneous province? Journal of Petrology 42, 731–763.

Kröner, A., Wilde, S. A., Li, J. H., Wang, K. Y., 2005. Age and evolution of a late Archean to early Palaeozoic upper to lower crustal section in the Wutaishan/Hengshan/Fuping terrain of northern China. Journal of Asian Earth Sciences 24, 577–595.

Kusky, T. M., Li, J. H., 2003. Paleoproterozoic tectonic evolution of the North China Craton. Journal of Asian Earth Sciences 22, 383–397.

Lappin, M.A., Dawson, B.D., 1975. Two Roberts-Victor cumulate eclogites and their re-equilibration. Physics and Chemistry of the Earth 9, 351–365.

Li, Q.L., Wu, F.Y., Li, X.H., Qiu, Z.L., Liu, Y., Yang, Y.H., Tang, G.Q., 2011. Precisely dating Paleozoic kimberlites in the North China Craton and Hf isotopic constraints on the evolution of the subcontinental lithospheric mantle. Lithos 126, 137-134.

Li, S.G., Hart, S.R., Zheng, S., Liou, D., Zhang, G. and Guo, A., 1989. Timing of collision between the North and South China Blocks: Sm-Nd isotopic age evidence. Science in China (Series B) 32, 1391–1400.

Liu, D. Y., Nutman, A. P., Compston, W., Wu, J. S., Shen, Q. H., 1992. Remnants of 3800 Ma crust in Chinese part of the Sino-Korean craton. Geology 20, 339–342.

Liu, S., Li, S., Guo, S., Hou, Z., He, Y., 2012. The Cretaceous adakitic–basaltic–granitic magma sequence on south-eastern margin of the North China Craton: Implications for lithospheric thinning mechanism. Lithos 134-135, 163–178.

Liu, S.W., Santosh, M., Wang, W., Bai, X., Yang, P., 2011a. Zircon U–Pb chronology of the Jianping Complex: Implications for the Precambrian crustal evolution history of the northern margin of North China Craton. Gondwana Research 20, 48–63.

Liu, Y.-C., Li, S., Gu, X., Hou, Z., 2006. Zircon SHRIMP U-Pb dating for olivine gabbro at Wangmuguan in the Beihuaiyang zone and its geological significance. Chinese Science Bulletin 51, 2500–2506.

Liu, Y.-C, Li, S., Gu, X., Xu, S., Chen, G., 2007. Ultrahigh-pressure eclogite transformed from mafic granulite in the Dabie orogen, east-central China. Journal of Metamorphic Geology 25, 975–989.

Liu, Y.-C., Wang, A., Rolfo, F., Groppo, C., Gu, X., Song, B., 2009. Geochronological and petrological constraints on Palaeoproterozoic granulite facies metamorphism in southeastern margin of the North China Craton. Journal of Metamorphic Geology 27, 125–138.

Liu, Y.-C., Gu, X., Li, S., Hou, Z., Song, B., 2011b. Multistage metamorphic events in granulitized eclogites from the North Dabie complex zone, central China: evidence from zircon U-Pb age, trace element and mineral inclusion. Lithos 122, 107–121.

Liu, Y.S., Gao, S., Yuan, H.L., Zhou, L., Liu, X., Wang, X.C., Hu, Z.C., Wang, L.S., 2004. U–Pb zircon ages and Nd, Sr, and Pb isotopes of lower crustal xenoliths from North China Craton: insights on evolution of lower continental crust. Chemical Geology 211, 87–109.

Loock, G., Stosch, H. G., Seck, H. A., 1990. Granulite facies lower crustal xenoliths from the Eifel, West Germany: petrological and geochemical aspects. Contributions to Mineralogy and Petrology 105, 25–41.

Ludwig, K. R., 2001. User's Manual for Isoplot/Ex (rev. 2.49): a Geochronological Toolkit for Microsoft Excel. Berkeley Geochronology Center, Berkeley, CA, Special Publication 1a, 55 pp.

Manikyamba, C., Kerrich, R., 2011. Geochemistry of alkaline basalts and associated high-Mg basalts from the 2.7 Ga Penakacherla Terrane, Dharwar craton, India: An

Archean depleted mantle-OIB array. Precambrian Research 188, 104–122.

Martin, H., 1999. The adakitic magmas: modern analogues of Archaean granitoids. Lithos 46, 411–429.

Martin, H., Smithiesb, R.H., Rappc, R., Moyend, J.-F., Champion, D., 2005. An overview of adakite, tonalite–trondhjemite–granodiorite (TTG), and sanukitoid: relationships and some implications for crustal evolution. Lithos 79, 1–24.

Mattauer, M., Matte, P., Malavieille, J., Tapponnier, P., Maluski, H., Ku, Z., Lu, Y., and Tang, Y., 1985. Tectonics of the Qinling Belt: Build-up and evolution of eastern Asia. Nature 317, 496–500.

Möller, A., O'Brien, P. J., Kennedy, A., Kröner, A., 2002. Polyphase zircon in ultrahigh-temperature granulites (Rogaland, SW Norway): constraints for Pb diffusion in zircon. Journal of Metamorphic Geology 20, 727–740.

Montanini, A., Harlov, D., 2006. Petrology and mineralogy of granulite-facies mafic xenoliths (Sardinia, Italy): Evidence for KCl metasomatism in the lower crust. Lithos 92, 588–608.

Moser, D. E., Heaman, L. M., 1997. Proterozoic zircon growth in Archean lower crustal xenoliths, southern Superior craton – a consequence of Matachewan ocean opening. Contributions to Mineralogy and Petrology 128, 164–175.

O'Brien, P. J., Rötzler, J., 2003. High-Pressure granulites: Formation, Recovery of peak conditions, and implications for tectonics. Journal of Metamorphic Geology 21, 3–20.

O'Neill, H. S. T., 1981. The transition between spinel lherzolite and garnet lherzolite, and its use as a geobarometer. Contributions to Mineralogy and Petrology 77, 185–194.

Otten, M. T., 1984. The origin of brown hornblende in the Artfället gabbro and dolerites. Contributions to Mineralogy and Petrology 86, 189–199.

Pattison, D. R. M., 2003. Petrogenetic significance of orthopyroxene-free garnet + clinopyroxene + plagioclase ± quartz-bearing metabasites with respect to the amphibolite and granulite facies. Journal of metamorphic Geology 21, 21–34.

Peng, S., Kusky, T.M., Jiang, X.F., Wang, L., Wang, J.P., Deng, H., 2012. Geology,

geochemistry, and geochronology of the Miaowan ophiolite, Yangtze craton: Implications for South China's amalgamation history with the Rodinian supercontinent. Gondwana Research 21, 577–594.

Raase, P., 1974. Al and Ti contents of hornblende, indicators of pressure and temperature of regional metamorphism. Contributions to Mineralogy and Petrology 45, 231–236.

Rogers, N.W., 1977. Granulite xenoliths from Lesotho kimberlite and the lower continental crust. Nature 270, 681–684.

Rudnick, R. L., McDonough, W. F., McCulloch, M. T., Taylor, S. R., 1986. Lower crust xenoliths from Queensland, Australia: evidence for deep crustal assimilation and fractionation of continental basalts. Geochimica Cosmochimica Acta 50, 1099–1115.

Rudnick, R. L., 1995. Making continental crust. Nature 378, 571–578.

Sajona, F.G., Maury, R., Bellon, H., Cotten, J., Defant, M.J., 1996. High field strength element enrichment of Pliocene–Pleistocene island arc basalts, Zamboanga Peninsula, western Mindanao (Philippines). Journal of Petrology 37, 693–726.

Santosh, M., 2010. Assembling North China Craton within the Columbia supercontinent: the role of double-sided subduction. Precambrian Research 178, 149–167.

Santosh, M., Tsunogae, T., Li, J.H., Liu, S.J., 2007a. Discovery of sapphirine-bearing Mg-Al granulites in the North China Craton: implications for Paleoproterozoic ultrahigh-temperature metamorphism. Gondwana Research 11, 263–285.

Santosh, M., Wilde, S., Li, J.H., 2007b. Timing of Paleoproterozoic ultrahigh-temperature metamorphism in the North China Craton: evidence from SHRIMP U-Pb zircon geochronology. Precambrian Research 159, 178–196.

Sautter, V., Harte, B., 1988. Diffusion gradients in an eclogite xenolith from the Roberts Victor kimberlite pipe: 1. Mechanism and evolution of garnet exsolution in Al_2O_3-rich clinopyroxenes. Journal of Petrology 29, 1325–1352.

Shaw, D.M., 1972. The origin of the Apsley gneiss, Ontario. Canadian Journal of Earth Sciences 9, 18–35.

Sobolev, V. S., Sobolev, N. V., 1964. Xenoliths in kimberlites of northern Yakutia and the structure of the mantle. Doklady Akademeii Nauk SSSR (Series Geologi) 158, 22–26.

Soderlund, U., Patchett, P.J., Vervoort, J.D., Isachsen, C.E., 2004. The ^{176}Lu decay constant determined by Lu-Hf and U-Pb isotope systematics of Precambrian mafic intrusions. Earth and Planetary Science Letters 219, 311–324.

Stolz, A. J., Davies, G. R., 1989. Metasomatised lower crustal and upper mantle xenoliths from north Queensland: chemical and isotopic evidence bearing on the composition and source of the fluid phase. Geochimica et Cosmochimica Acta 53, 649–660.

Stosch, H.-G., Lugmair, G. W., 1984. Evolution of the lower continental crust: granulite facies xenoliths from the Eifel. Nature 311, 368–370.

Sun, S. S., McDonough, W. F., 1989. Chemical and isotopic systematics of oceanic basalts: implications for mantle composition and processes. In: Saunders, A. D. & Norry, M. J. (eds) Magmatism in the Ocean Basins. Geological Society, London, Special Publications 42, 313–345.

Tang, J., Zheng, Y.F., Wu, Y.B., Gong, B., Liu, X.M., 2007. Geochronology and geochemistry of metamorphic rocks in the Jiaobei terrane: constraints on its tectonic affinity in the Sulu orogen. Precambrian Research 152, 48–82.

Upton, B.G.J., Aspen, P., Hinton, R.W., 2001. Pyroxenite and granulite xenoliths from relationships beneath the Scottish Northern Highlands Terrane: evidence for lower crustal–upper mantle relationships. Contributions to Mineralogy and Petrology 142, 178–197.

Vavra, G., Gebauer, D., Schmid, R., Compston, W., 1996. Multiple zircon growth and recrystallization during polyphase Late Carboniferous to Triassic metamorphism in granulites of the Ivrea Zone (Southern Alps): an ion microprobe (SHRIMP) study. Contributions to Mineralogy and Petrology 122, 337–358.

Vervoort, J. D., Blichert-Toft, J., 1999. Evolution of the depleted mantle: Hf isotope evidence from juvenile rocks through time. Geochimica et Cosmochimica Acta 63, 533–556.

Wang, Q., Wyman, D.A., Xu, J. F., Wan, Y. S., Li, C. F., Zi, F., Jiang, Z. Q., Qiu, H. N., Chu, Z. Y., Zhao, Z. H., Dong, Y. H., 2008. Triassic Nb-enriched basalts, magnesian andesites, and adakites of the Qiangtang terrane (Central Tibet): evidence for metasomatism by slab-derived melts in the mantle wedge. Contributions to Mineralogy and Petrology 155, 473–490.

Weber, M. B. I., Tarney, J., Kempton, P. D., Kent, R. W., 2002. Crustal make-up of the northern Andes, evidence based on deep crustal xenolith suites, Mercadaeres, SW Colombia. Tectonophysics 345, 49–82.

White, R. S., Spence, G. D., Fowler, S. R., McKenzie, D. P., Westbrook, G. K., Bowen, A. N., 1987. Magmatism at rifted continental margins. Nature 330, 439–444.

Whitney, D.L., Evans, B.W., 2010. Abbreviations for names of rock-forming minerals. American Mineralogist 95, 185–187.

Wilde, S.A., Zhao, G.C., Sun, M., 2002. Development of the North China Craton during the late Archaean and its final amalgamation at 1.8 Ga: Some speculations on its position within a global Palaeoproterozoic supercontinent. Gondwana Research 5, 85–94.

Williams, I. S., 1998. U–Th–Pb geochronology by ion microprobe, *in* McKibben, M.A., and Shanks III, W.C., Ridley, W.I., eds, Applications of Microanalytical Techniques to Understanding Mineralizing Processes. Reviews in Economic Geology 7, 1–35.

Winchester, J.A., Floyd, P.A., 1977. Geochemical discrimination of different magma series and their differentiation products using immobile elements. Chemical Geology 20, 325–343.

Woodhead, J., Hergt, J., Shelley, M., Eggins, S., Kemp, R., 2004. Zircon Hf-isotope analysis with an excimer laser, depth profiling, ablation of complex geometries, and concomitant age estimation. Chemical Geology 209, 121–135.

Woodhead, J. D., Hergt, J. M., 2005. A preliminary appraisal of seven natural zircon reference materials for in situ Hf isotope determination. Geostandards and Geoanalytical Research 29, 183–195.

Wu, F.Y., Zhao, G.C., Wilde, S.A., Sun, D.Y., 2005. Nd isotopic constraints on crustal formation in the North China Craton. Journal of Asian Earth Sciences 24, 523–545.

Wu, F. Y., Yang, Y. H., Xie, L. W., Yang, J. H., Xu, P., 2006. Hf isotopic compositions of the standard zircons and baddeleyites in U-Pb geochronology. Chemical Geology 234, 105–126.

Wu, F. Y., Zhang, Y. B., Yang, J. H., Xie, L. W., Yang, Y. H., 2008. Zircon U-Pb and Hf isotopic constraints on the Early Archean crustal evolution in Anshan of the North China Craton. Precambrian Research 167, 339–362.

Xu, X.S., O'Reilly, S.Y., Griffin, W.L., Zhou, X.M., Huang, X.L., 1998. The nature of the Cenozoic lithospheric beneath Nushan, East Central China. In Mantle Dynamics and Plate Interaction in East Asian. AGU Geodynamics Series 27, 167-196.

Xu, P., Wu, F. Y., Xie, L. W., Yang, Y. H., 2004. Hf isotopic compositions of the standard zircons for U–Pb dating. Chinese Science Bulletin 49, 1642–1648.

Xu, W. L., Wang, D.Y., Liu, X. C., Wang, Q. H., Lin, J. Q., 2002. Discovery of eclogite inclusions and its geological significance in early Jurassic intrusive complex in Xuzhou-northern Anhui, eastern China. Chinese Science Bulletin 47, 1212–1216.

Xu, W. L., Gao, S., Wang, Q., Wang, D., Liu, Y., 2006. Mesozoic crustal thickening of the eastern North China craton: Evidence from eclogite xenoliths and petrologic implications. Geology 34, 721–724.

Xu, W. L., Gao, S., Yang, D., Pei, F., Wang, Q., 2009. Geochemistry of eclogite xenoliths in Mesozoic adakitic rocks from Xuzhou-Suzhou area in central China and their tectonic implications. Lithos 107, 269–280.

Yardley, B. W. D., 1989. An introduction to Metamorphic Petrology. Longman Group, Harlow, UK, pp. 49-51.

Yogodzinski, G. M., Kay, R. W., Volynets, O. N., Koloskov, A. V., Kay, S. M., 1995. Magnesian andesites in the western Aleutian Komandorsky region: implication

for slab melting and metasomatic processes in the mantle wedge. Geological Society of America Bulletin 107, 505–519.

Yu, J.H., Xu, X.S., O'Reilly, S.Y., Zhang, M., 2003. Granulite xenoliths from Cenozoic Basalts in SE China provide geochemical fingerprints to distinguish lower terranes from the North and South China tectonic blocks. Lithos 67, 77-102.

Zeh, A., Gerdes, A., Barton, J. M., Jr. 2009. Archean Accretion and Crustal Evolution of the Kalahari Craton—the Zircon Age and Hf Isotope Record of Granitic Rocks from Barberton/Swaziland to the Francistown Arc. Journal of Petrology 50, 933–966.

Zhai, M. G., Bian, A. G., Zhao, T. P., 2000. The amalgamation of the supercontinent of North China craton at the end of the Neoarchaean, and its break-up during the late Palaeoproterozoic and Mesoproterozoic. Science in China (Series D) 43 (Supplement), 219–232.

Zhai, M. G., Liu, W. J., 2003. Palaeoproterozoic tectonic history of the North China Craton: a review. Precambrian Research 122, 183–99.

Zhai, M.G., Guo, J.H., Liu,W.J., 2005. Neoarchean to Paleoproterozoic continental evolution and tectonic history of the North China Craton. Journal of Asian Earth Sciences 24, 547–561.

Zhai, M., Santosh, M., 2011. The early Precambrian odyssey of the North China Craton: A synoptic overview. Gondwana Research 20, 6–25.

Zhai, X.M., Day, H.W., Hacker, B.R., You, Z., 1998. Palezoic metamorphism in the Qinling orogen, Tongbai Mountains, central China. Geology 26, 37 l–374.

Zhang, H.F., Sun, M., Zhou, X.H., Fan, W.M., Zhai, M.G. and Yin, J.F., 2002. Mesozoic lithosphere destruction beneath the North China Craton: evidence from major-, trace-element and Sr-Nd-Pb isotope studies of Fangcheng basalts. Contributions to Mineralogy and Petrology 144, 241-253.

Zhang, H.F., 2005. Transformation of lithospheric mantle through peridotite-melt reaction: a case of Sino-Korean craton. Earth and Planetary Science Letters 237, 768-780.

Zhang, H.F., 2012. Destruction of ancient lower crust through magma underplating beneath Jiaodong Peninsula, North China Craton: U–Pb and Hf isotopic evidence from granulite xenoliths. Gondwana Research 21, 281–292.

Zhang, H.F., Ying, J.F., Santosh, M., Zhao, G.C., 2012. Episodic growth of Precambrian lower crust beneath the North China Craton: A synthesis. Precambrian Research, DOI: 10.1016/j.precamres.2011.04.006.

Zhao, G. C., Cawood, P.A., Wilde, S. A., Sun, M., Lu, L., 2000. Metamorphism of basement rocks in the Central Zone of the North China craton: implications for Palaeoproterozoic tectonic evolution. Precambrian Research 103, 55–88.

Zhao, G., Wilde, S. A., Cawood, P.A., Sun, M., 2001. Archean blocks and their boundaries in the North China craton: lithological, geochemical, structural, and P–T path constraints and tectonic evolution. Precambrian Research 107, 45–73.

Zheng, J., Sun. M., Lu, F., Pearson, N., 2003. Mesozoic lower crustal xenoliths and their significance in lithospheric evolution beneath the Sino-Korean Craton. Tectonophysics 361, 37–60.

Zheng, J.P., Griffin,W.L., O'Reilly, S.Y., Lu, F.X., 2004a. 3.6 Ga lower crust in central China: new evidence on the assembly of the North China Craton. Geology 32, 229–232.

Zheng, J.P., Griffin, W.L., O'Reilly, S.Y., Lu, F.X., Yu, C.M., 2004b. U–Pb and Hf-Isotope analysis of zircons in mafic xenoliths from Fuxian kimberlites: evolution of the lower crust beneath the North China Craton. Contributions to Mineralogy and Petrology 148, 79–103.

Zheng, J.P., Griffin,W.L., O'Reilly, S.Y., Zhao, J.H.,Wu, Y.B., Liu, G.L., Pearson, N., Zhang, M., Ma, C.Q., Zhang, Z.H., Yu, C.M., Su, Y.P., Tang, H.Y., 2009. Neoarchean (2.7–2.8 Ga) accretion beneath theNorth China Craton: U–Pb age, trace elements and Hf isotopes of zircons in diamondiferous kimberlites. Lithos 112, 188–202.

Zheng, Y.-F., Zhao, Z.-F., Wu, Y.-B., Zhang, S.-B., Liu, X.-M., Wu, F.-Y., 2006. Zircon U – Pb age, Hf and O isotope constraints on protolith origin of

ultrahigh-pressure eclogite and gneiss in the Dabie orogen. Chemical Geology 231, 135–158.

Zhou, X., Yu, J.H., Xu, X., 1992. Discovery and significance of granulite xenoliths in Nushan basalt, East China. Chinese Science Bulletin 37, 1730–1734.

Figure captions

Figure 1 Schematic geological map of the Qinling–Dabie–Sulu collision zone and adjacent parts of the North China Craton (modified after Xu *et al*., 2006), with inset showing the major tectonic divisions of China and the location of the study area. YZ and SC denote the Yangtze Craton and South China Orogen, respectively. Also shown are the subdivisions of the North China Craton (Zhao *et al*., 2000), where WB, TNCO and EB denote the Western Block, Trans-North China Orogen and Eastern Block, respectively.

Figure 2 Photographs showing the field occurrence of deep-seated xenoliths of spinel-bearing garnet clinopyroxenite (a), garnet granulite (b), garnet amphibolite (c) and basic gneiss (d) in the Mesozoic dioritic porphyry at Jiagou near Suzhou.

Figure 3 Microstructures of deep-seated xenoliths from Jiagou in the southeastern margin of the North China Craton. (a) Garnet corona surrounding spinel and oriented garnet needles in clinopyroxene, spinel-bearing garnet clinopyroxenite (sample 07JG03) , plane polarized light (PPL); (b) Oriented garnet needles in clinopyroxene, spinel-bearing garnet clinopyroxenite (sample 07JG30), PPL; (c) Phlogopite and intergrowth of clinopyroxene + phlogopite + K-feldspar in phlogopite clinopyroxenite (sample 08JG06), PPL; (d) Clinopyroxene inclusion in garnet and its transformation to a symplectite of hornblende + plagioclase in the matrix, garnet granulite (sample 08JG15), PPL; (e) Back scattered electron (BSE) image showing clinopyroxene (darker) partially replaced by hornblende; K-feldspar and plagioclase occur in the fractures, garnet-bearing amphibolite (sample 07JG12); (f) Garnet + plagioclase + hornblende + ilmenite after rutile, garnet-bearing hornblende-plagioclase gneiss (sample 07JG32), PPL.

Figure 4 SiO_2–Zr/TiO_2 diagram (after Winchester and Floyd, 1977) for the studied xenoliths in the Mesozoic dioritic porphyry at Jiagou. Symbols used for the three

groups of xenoliths are the same as in the following figures.

Figure 5 SiO_2–Mg# (a) and Nb–Mg# (b) diagrams for the deep-seated xenoliths from Jiagou. HNB and NEB denote high-Nb basalt and Nb-enriched basalt, respectively based on Sajona et al. (1996) and Martin et al. (2005). Symbols as in Fig. 4.

Figure 6 Chondrite-normalized rare earth element diagrams for Groups 1 (a), 2 (b) and 3 (c) of the xenoliths from Jiagou. Normalization values are from Sun and McDonough (1989).

Figure 7 Primitive-mantle-normalized spider diagrams for Groups 1 (a), 2 (b) and 3 (c) of the xenoliths from Jiagou. Normalization values are from Sun and McDonough (1989).

Figure 8 Sr/Y–Y diagram (Defant and Drummond, 1990; Martin, 1999) for Groups 2 and 3 of the xenoliths from Jiagou.

Figure 9 Plot of Ba–Nb/Y for the deep-seated xenoliths from Jiagou. Symbols as for Fig. 4.

Figure 10 Cathodoluminescene (CL) images for zircon from samples 07JG30 (a–c), 07JG34 (d–k) and 07JG32 (l–p). The open circles are spot analysis with available $^{206}Pb/^{238}U$ ages.

Figure 11 Zircon SHRIMP U-Pb dating for the xenoliths from samples 07JG30 (a), 07JG34 (b) and 07JG32 (c) at Jiagou. All errors are given at 2σ level.

Figure 12 Histograms of single-stage depleted mantle Hf model ages (T_{DM1}) for the zircons from sample 07JG30 (a) and two-stage depleted mantle Hf model ages (T_{DM2}) for the zircons from samples 07JG34 (b), 07JG12 (c), 07JG14 (d) and 07JG32 (e) of

the xenoliths at Jiagou and the exposed meta-basement (sample 07FY01) (f) at Bengbu.

Figure 13 The relationship between U-Pb age and $\varepsilon_{Hf}(t)$ values for the igneous core and metamorphic rim of zircons as identified by the SHRIMP U-Pb dating for four xenoliths (samples 07JG34, 07JG12, 07JG14 and 07JG32) from Jiagou and one garnet amphibolite (sample 07FY01) from the exposed basement at Bengbu. Deleted Mantle (DM) and CHUR evolution lines are also shown. The solid and open spots for different samples denote ε_{Hf} (t) values at their precursor and corresponding metamorphic ages, respectively. Dashed arrow lines indicate the core–rim analyses of zircons with the arrow pointing to the rim.

Table 1

Table 1 Electron microprobe analyses (wt. %) of representative minerals from the xenoliths at Jiagou in the southeastern margin of the North China Craton

Mineral	Garnet			Pyroxene				Amphibole		Phlogopite		Feldspar	
Sample	07JG03	07JG03	07JG30	07JG03	07JG30	08JG06	08JG15	07JG30	08JG15	08JG06	08JG06	07JG12	07JG12
Site	m	i	i	m	m	m	i	m	m	Sy	m	Sy	Sy
SiO_2	38.91	38.98	38.88	51.10	49.66	53.23	52.58	40.80	43.78	39.10	39.77	65.08	62.92
TiO_2	0.00	0.00	0.11	0.00	1.23	0.03	0.12	1.12	0.51	2.02	1.89	0.00	0.00
Al_2O_3	21.84	21.62	21.79	4.11	7.72	1.71	2.77	17.08	11.55	13.85	15.37	18.45	23.12
Fe_2O_3	1.77	1.83	0.86	3.85	0.00	0.00	0.00					0.00	0.00
FeO	16.59	16.95	14.68	1.97	5.32	5.67	8.88	9.94	18.01	11.56	11.77	0.00	0.00
MnO	0.00	0.00	0.00	0.00	0.05	0.11	0.10	0.00	0.12	0.07	0.06	0.00	0.00
MgO	5.24	5.55	3.84	14.83	11.61	14.40	12.46	12.19	9.91	18.81	16.59	0.00	0.00
CaO	16.08	15.43	19.51	23.60	22.71	24.43	21.37	11.99	10.88	0.06	0.01	0.00	4.80
Na_2O	0.00	0.00	0.00	0.53	1.42	0.27	1.36	2.75	1.80	0.08	0.13	1.80	8.58
K_2O	0.00	0.00	0.00	0.00	0.01	0.02	0.00	1.07	0.75	8.94	10.17	14.65	0.57
Total	100.43	100.36	99.67	99.99	99.73	99.87	99.64	96.94	97.31	94.49	95.76	99.98	99.99
O	12	12	12	6	6	6	6	23	23	12	12	8	8
Si	2.97	2.97	2.99	1.88	1.83	1.97	1.96	6.01	6.49	2.90	2.88	2.98	2.79
Al^{IV}	0.03	0.02	0.01	0.12	0.17	0.03	0.04	1.02	1.00	1.32	1.20	1.00	1.21
Al^{VI}	1.93	1.92	1.95	0.05	0.16	0.04	0.08	0.97	0.51				
Fe^{3+}	0.10	0.10	0.05	0.10	0.04	0.01	0.06	0.00	0.78			0.00	0.00
Ti	0.00	0.00	0.00	0.00	0.00	0.00	0.00	0.12	0.06	0.10	0.11	0.00	0.00
Fe^{2+}	1.06	1.08	0.94	0.06	0.12	0.16	0.22	1.22	1.46	0.72	0.71	0.00	0.00
Mg	0.59	0.63	0.44	0.81	0.64	0.79	0.69	2.68	2.19	1.80	2.06	0.00	0.00
Mn	0.00	0.00	0.00	0.00	0.00	0.00	0.00	0.00	0.01	0.00	0.00	0.00	0.00
Ca	1.31	1.26	1.60	0.93	0.89	0.97	0.85	1.89	1.73	0.00	0.00	0.00	0.23
Na	0.00	0.00	0.00	0.04	0.10	0.02	0.10	0.78	0.52	0.02	0.01	0.16	0.74
K	0.00	0.00	0.00	0.00	0.00	0.00	0.00	0.20	0.14	0.95	0.84	0.86	0.03

Note: m, matrix; i, inclusion or exsolution; Sy, symplectite. Garnet/pyroxene stoichiometries and the amount of Fe^{3+} and Fe^{2+} were estimated on the base of eight/four cations and the charge-balance constraint; Fe^{3+} content in amphibole was calculated as Si + Al + Ti + Mg + Fe + Mn = 13 for O = 23.

Table 2

Table 2 Major and trace element compositions of the xenoliths from Jiagou in the southeastern margin of the North China Craton. Major oxides are in wt. %, trace elements in ppm.

Type	Group 1						Group 2		
Sample	07JG03	07JG17	07JG21	07JG30	08JG06	08JG09	07JG05-2	07JG06	07JG07
SiO_2	42.88	46.06	48.08	42.02	47.42	45.4	46.08	52.72	39.10
Al_2O_3	11.80	9.29	6.45	13.24	17.62	9.96	12.18	16.89	14.90
Fe_2O_3	3.17	1.66	3.79	3.21	1.67	2.58	6.24	2.80	7.90
TiO_2	1.02	1.27	0.48	1.04	1.04	0.64	1.98	0.38	3.01
FeO	7.33	7.07	8.45	7.59	6.32	5.13	10.35	6.87	11.86
CaO	17.36	20.48	13.83	18.52	7.00	19.93	12.31	6.06	7.79
MgO	11.64	11.32	14.63	9.75	8.00	14.02	5.90	6.65	9.56
K_2O	0.5	0.07	0.26	0.21	5.55	0.06	0.59	0.73	0.89
Na_2O	1.16	0.93	1.23	0.99	2.00	0.44	1.71	4.03	1.65
MnO	0.14	0.14	0.23	0.15	0.07	0.09	0.21	0.18	0.44
P_2O_5	0.03	0.07	0.06	0.02	0.13	0.05	0.33	0.04	0.06
H_2O^+	1.14	0.36	0.74	0.73	1.55	0.62	0.68	2.26	2.09
LOI	2.88	1.66	2.09	2.77	2.8	2.14	2.22	3.09	3.03
Mg#	67	70	69	62	65	77	40	56	47
Cr	3.99	42.24	447.4	93.7	136.1	36.1	46.8	97.5	163.4
Ni	21.8	18.4	178.7	64.2	24.0	173.0	76.1	90.5	48.4
Rb	20.6	0.87	1.43	11.5	76.3	1.26	29.8	27.4	13.5
Sr	119.9	57.4	91.8	57.7	196.8	88.4	218.9	573.9	218.9
Y	15.4	18.9	15.1	13.8	20.9	12.6	79.9	6.37	77.7
Zr	99.0	103.0	68.0	83.9	68.7	202.9	248.0	38.8	46.2
Nb	2.08	1.27	1.34	2.54	3.96	1.86	42.3	1.32	4.21
Ba	190.6	19.4	34.3	100.6	1425.5	22.4	127.6	279.6	214.6
La	4.79	3.54	19.89	2.21	6.51	10.7	35.0	7.74	6.72
Ce	10.9	9.88	42.3	6.56	14.0	30.3	89.4	13.5	13.6
Pr	1.34	1.35	5.16	0.87	1.86	4.13	13.50	1.43	1.76
Nd	6.37	7.06	22.5	4.69	9.34	18.7	72.4	6.54	9.57
Sm	1.75	2.19	4.37	1.51	2.73	3.82	21.10	1.37	3.60
Eu	0.54	0.63	1.04	0.44	0.83	0.57	3.32	1.16	1.23
Gd	2.20	2.80	4.25	1.95	3.15	3.18	20.6	1.43	6.11
Tb	0.36	0.47	0.51	0.34	0.53	0.40	2.69	0.18	1.26
Dy	2.39	3.17	2.82	2.39	3.45	2.09	14.2	1.08	9.96
Ho	0.51	0.68	0.52	0.52	0.73	0.38	2.55	0.21	2.48
Er	1.45	1.95	1.44	1.51	2.06	1.06	6.75	0.59	7.90
Tm	0.22	0.30	0.20	0.23	0.28	0.14	0.96	0.09	1.32
Yb	1.61	2.14	1.44	1.65	1.78	0.94	6.80	0.66	10.30
Lu	0.25	0.33	0.21	0.25	0.26	0.14	1.02	0.10	1.68
Hf	1.57	2.26	1.70	1.77	1.67	3.83	5.79	0.75	1.08
Ta	0.30	0.29	0.13	0.39	0.20	0.55	2.23	0.07	0.25
Pb	66.9	21.6	56.1	110.0	14.7	5.34	23.2	29.6	38.5

Th	0.73	0.63	0.30	0.42	0.99	2.02	7.93	0.09	0.94
U	3.74	1.01	1.04	0.26	2.95	2.60	2.62	0.32	3.04
Type			Group 2				Group 3		
Sample	07JG12	07JG14	07JG29	07JG34	08JG08	08JG15	07JG32	08JG03	
SiO_2	43.48	48.46	37.92	51.3	46.68	45.8	53.58	67.06	
Al_2O_3	10.84	12.59	12.81	14.28	15.65	13.09	15.64	15.46	
Fe_2O_3	6.61	1.87	8.51	3.20	3.23	3.82	4.08	0.88	
TiO_2	5.21	1.70	1.95	1.33	1.47	1.03	0.53	0.21	
FeO	12.48	14.99	10.73	8.33	11.86	13.89	5.77	1.70	
CaO	7.79	10.44	8.43	7.95	10.92	11.24	8.37	3.60	
MgO	7.92	7.17	11.97	5.18	5.10	6.78	5.48	1.29	
K_2O	0.48	0.11	0.91	1.3	0.28	0.37	0.48	1.79	
Na_2O	2.21	0.79	1.84	3.96	2.84	1.8	3.77	5.86	
MnO	0.26	0.30	0.21	0.19	0.27	0.30	0.17	0.04	
P_2O_5	0.12	0.05	0.03	0.36	0.19	0.16	0.019	0.11	
H_2O^+	1.56	0.47	6.06	1.45	0.80	0.45	1.61	0.89	
LOI	2.76	1.72	3.69	2.51	1.79	1.92	2.16	1.37	
Mg#	43	43	54	45	39	41	51	48	
Cr	252.4	25.9	97.7	80.0	62.4	78.7	202.1	79.4	
Ni	247.7	109.7	47.2	98.3	21.6	92.0	96.8	29.5	
Rb	3.97	1.42	8.77	23.8	2.00	3.68	6.46	38.7	
Sr	297.9	76.2	225.9	833.8	235.8	253.8	421.8	1473	
Y	14.9	37.2	18.5	22.3	25.0	35.8	14.8	4.98	
Zr	72.2	30.1	23.0	115.9	92.6	79.8	49.9	96.5	
Nb	15.4	2.92	2.20	9.39	8.17	4.13	2.24	5.11	
Ba	74.7	26.2	147.6	476.5	52.5	89.7	93.4	1299	
La	7.42	11.7	8.68	36.4	11.4	7.92	12.7	8.94	
Ce	17.5	19.2	14.7	80.3	24.9	16.6	19.2	17.4	
Pr	2.33	2.16	1.79	9.84	3.23	2.06	3.13	1.94	
Nd	11.7	9.76	9.45	42.8	15.6	10.3	14.2	8.06	
Sm	2.94	2.74	2.71	8.20	4.15	3.23	3.07	1.62	
Eu	0.99	1.04	0.91	1.66	1.46	0.96	0.90	0.53	
Gd	3.11	4.07	3.16	6.63	4.51	4.14	2.87	1.31	
Tb	0.43	0.75	0.49	0.77	0.71	0.73	0.40	0.15	
Dy	2.49	5.41	3.12	3.82	4.30	4.91	2.34	0.79	
Ho	0.48	1.25	0.66	0.67	0.88	1.09	0.47	0.15	
Er	1.31	3.65	1.85	1.84	2.48	3.25	1.35	0.46	
Tm	0.19	0.57	0.27	0.23	0.35	0.49	0.19	0.07	
Yb	1.36	4.16	1.81	1.51	2.28	3.32	1.27	0.46	
Lu	0.21	0.65	0.27	0.22	0.35	0.52	0.20	0.07	
Hf	1.62	0.87	0.70	2.35	2.26	1.80	1.09	2.56	
Ta	0.73	0.09	0.12	0.34	0.53	0.24	0.07	0.17	
Pb	15.7	4.06	75.5	20.2	1.56	6.05	13.8	27.6	
Th	0.21	0.36	0.37	0.71	1.18	0.74	0.29	1.51	

U	0.74	0.34	1.10	1.86	0.38	0.97	0.11	1.07

Table 3

Table 3 Electron microprobe analyses (wt. %) of representative minerals in zircon from the xenoliths at Jiagou in the southeastern margin of the North China Craton

Mineral	Garnet	Diopside	Rutile	Plagioclase		
No.	07JG32	07JG34	07JG32	07JG32		07JG34
Site	Zir-R	Zir-R	Zir-R	Zir-R	Zir-R	Zir-R
SiO_2	39.24	50.62	0.28	58.75	59.62	60.65
TiO_2	0.00	0.21	98.72	0.00	0.00	0.01
Al_2O_3	22.11	3.83	0.00	25.97	25.56	24.64
FeO*	24.90	11.49	0.88	0.04	0.04	0.06
MnO	0.80	0.18	0.03	0.02	0.00	0.04
MgO	6.04	11.21		0.04	0.03	0.03
CaO	6.76	21.24		8.13	7.26	6.29
Na_2O	0.00	1.15		6.87	7.17	7.54
K_2O	0.01	0.00		0.16	0.21	0.57
Total	99.95	99.96	99.91	99.98	99.89	99.83
O	12	6		8	8	8
Si	3.01	1.94		2.63	2.66	2.70
Al^{IV}	0.00	0.06		1.37	1.34	1.29
Al^{VI}	1.91	0.04				
Fe^{3+}	0.06	0.07		0.00	0.00	0.00
Ti	0.00	0.00		0.00	0.00	0.00
Fe^{2+}	1.80	0.18		0.00	0.00	0.00
Mg	0.55	0.78		0.00	0.00	0.00
Mn	0.10	0.00		0.00	0.00	0.00
Ca	0.56	0.88		0.39	0.35	0.30
Na	0.00	0.05		0.59	0.62	0.65
K	0.00	0.00		0.01	0.01	0.03

Note: Zir-R denotes the rim domain of zircon. Garnet/pyroxene stoichiometries and the amount of Fe^{3+} and Fe^{2+} were estimated based on eight/four cations and the charge-balance constraint. * represent all Fe.

Table 4

Table 4 SHRIMP zircon U-Pb data for the xenoliths at Jiagou in the southeastern margin of the North China Craton

Sample 07JG30

spot	$^{206}Pb_c$ %	U ppm	Th ppm	Th/U	$^{206}Pb^*$ ppm	$^{207}Pb^*/^{235}U$	±%	$^{206}Pb^{*/238}U$	±%	$^{206}Pb/^{238}U$ Age(Ma)	±1σ
1.1	7.49	264	127	0.48	15.4	0.68	23	0.0629	2.5	393	10
2.1	1.13	506	48	0.10	56.1	1.265	3.9	0.1276	2.5	774	18
3.1	1.93	288	171	0.60	15.5	0.487	16	0.0614	2.3	384	8.6
4.1	0.15	800	86	0.11	97.1	1.429	2.7	0.1411	2.0	851	16
5.1	1.64	491	293	0.60	27.2	0.481	11	0.0634	2.2	397	8
6.1	0.33	255	130	0.51	59.5	4.00	2.6	0.2699	2.1	1541	29
7.1	1.59	444	129	0.29	25.4	0.474	8.2	0.0656	2.6	410	10
8.1	1.79	458	274	0.60	24.9	0.612	12	0.0622	2.2	389	8
9.1	5.38	285	159	0.56	16.2	0.62	16	0.0625	2.5	391	9
10.1	3.10	566	335	0.59	34.2	0.71	16	0.0681	2.3	425	10
11.1	2.97	286	343	1.20	18.8	0.660	12	0.0744	2.2	462	10
4.2	0.16	1058	121	0.11	111	1.191	2.8	0.1220	2.0	742	14

Sample 07JG34

spot	$^{206}Pb_c$ %	U ppm	Th ppm	Th/U	$^{206}Pb^*$ ppm	$^{207}Pb^*/^{235}U$	±%	$^{206}Pb^{*/238}U$	±%	$^{207}Pb/^{206}Pb$ Age(Ma)	±1σ
1.1	0.00	13	16	1.23	3.91	7.91	5.4	0.358	4.2	2458	57
2.1	0.37	21	35	1.67	9.67	12.73	3.9	0.529	3.2	2602	38
3.1	0.64	34	56	1.65	14.50	11.02	4.0	0.491	2.6	2485	51
4.1	0.78	17	18	1.06	5.18	6.54	7.3	0.344	4.0	2203	110
5.1	0.93	22	48	2.18	9.15	11.50	6.1	0.488	3.9	2567	77
6.1	0.00	12	16	1.33	5.30	12.68	4.8	0.521	3.9	2622	46
7.1	1.83	11	12	1.09	4.22	9.45	7.1	0.445	4.1	2389	99
8.1	1.18	12	12	1.00	5.77	12.61	5.8	0.538	3.7	2559	74
9.1	0.00	13	23	1.77	4.10	6.95	6.8	0.362	5.0	2215	81
10.1	1.36	13	16	1.23	6.01	13.72	5.3	0.539	3.6	2696	65
11.1	1.26	14	19	1.36	5.33	10.49	6.5	0.452	4.2	2540	82
12.1	2.78	12	11	0.92	5.13	10.8	13	0.488	7.1	2466	190
13.1	1.18	11	11	1.00	5.30	14.11	5.5	0.560	4.1	2677	61
14.1	1.55	11	14	1.27	5.06	13.85	6.2	0.548	4.2	2683	75
15.1	0.19	147	9	0.06	51.80	8.20	1.4	0.4103	1.1	2287	16
16.1	1.72	23	20	0.87	6.52	6.02	7.7	0.329	3.1	2135	120
17.1	0.27	56	5	0.09	19.80	7.67	2.8	0.4125	2.0	2161	34
18.1	1.54	32	64	2.00	12.50	9.56	4.4	0.4467	2.2	2403	65
19.1	1.49	20	17	0.85	6.90	7.18	7.7	0.390	4.7	2148	110
20.1	1.34	12	15	1.25	4.76	12.42	7.8	0.469	3.3	2759	120
21.1	3.45	14	14	1.00	5.56	10.60	10	0.460	3.9	2526	160
22.1	1.34	13	17	1.31	4.10	6.61	11	0.359	3.7	2147	170

19.2	0.52	148	114	0.77	60.50	10.60	2.8	0.4736	1.0	2480	45

sample 07JG32

spot	$^{206}Pb_c$ %	U ppm	Th ppm	Th/U	$^{206}Pb^*$ ppm	$^{207}Pb^*/^{235}U$	±%	$^{206}Pb^{*}/^{238}U$	±%	$^{206}Pb/^{238}U$ Age(Ma)	±1σ
1.1	2.71	12	17	1.49	3.41	5.42	8.0	0.333	3.7	1853	59
2.1	0.20	78	117	1.49	25.7	6.84	2.6	0.3812	2.1	2082	38
3.1	5.84	21	26	1.23	6.37	4.47	15	0.330	3.5	1840	55
4.1	5.34	14	19	1.32	3.90	4.15	18	0.302	4.8	1700	72
5.1	2.62	7	16	2.34	2.12	6.41	9.1	0.344	4.8	1908	80
6.1	2.13	11	22	2.01	3.44	6.37	11	0.350	4.6	1937	76
7.1	2.92	21	21	1.02	5.82	4.91	8.8	0.318	3.2	1778	50
8.1	5.60	13	19	1.46	4.14	4.6	25	0.346	4.6	1918	74
9.1	1.49	20	42	2.09	5.71	5.18	7.1	0.321	3.2	1795	50
10.1	4.26	12	16	1.34	3.43	4.11	20	0.314	4.2	1761	63
11.1	0.71	52	32	0.62	14.3	5.00	4.3	0.3200	2.4	1790	37
12.1	1.14	63	75	1.18	21.8	6.90	3.7	0.3948	2.2	2145	41
13.1	0.31	194	223	1.15	65.3	7.12	2.2	0.3903	1.9	2124	34
14.1	6.38	27	27	1.00	7.90	4.61	15	0.319	3.3	1785	51
15.1	0.37	192	168	0.88	63.6	6.78	2.2	0.3836	2.0	2093	35
16.1	7.46	11	22	1.92	3.60	4.5	26	0.339	4.9	1881	77
17.1	1.49	38	28	0.74	9.92	4.37	8.0	0.2998	2.8	1690	42
18.1	0.60	99	58	0.58	34.3	7.34	2.8	0.3993	2.1	2166	38
19.1	0.60	24	21	0.89	7.19	5.97	5.4	0.351	3.2	1941	54
20.1	8.75	11	18	1.65	3.27	4.7	26	0.308	4.7	1729	68

Pb_c and Pb^* indicate the common and radiogenic portions, respectively. Pb^*: corrected for common ^{204}Pb using measured ^{204}Pb. All errors are 1σ. me - metamorphic zircon, ma - magmatic zircon, c - core, m - mantle, c - rim.

Table 5

Table 5 Hf isotopic compositions of zircons from the xenoliths at Jiagou in the southeastern margin of the North China Craton

No.	$^{176}Yb/^{177}Hf$	$^{176}Lu/^{177}Hf$	$^{176}Hf/^{177}Hf$	±(2σ)	Age (Ma)	$\varepsilon_{Hf(t2)}$ ±(2σ)	$\varepsilon_{Hf(t1)}$ ±(2σ)	T_{DM1} (Ma)	±(2σ)	$f_{Lu/Hf}$	T_{DM2} (Ma)	±(2σ)
Sample 07FY01 (t1 = 2100Ma, t2=1800Ma)												
1.1	0.000058	0.000003	0.281702	0.000024	1599	2.2±0.4	9.1±0.5	2120	32	-1.00	2132	53
5.1	0.000289	0.000009	0.281711	0.000021	1814	2.6±0.4	9.4±0.4	2107	28	-1.00	2111	45
6.1	0.000391	0.000011	0.281674	0.000022	1771	1.3±0.4	8.1±0.4	2157	30	-1.00	2193	48
12.1	0.000411	0.000012	0.281686	0.000021	1700	1.7±0.4	8.5±0.4	2141	28	-1.00	2167	46
13.1	0.000180	0.000005	0.281687	0.000017	1812	1.7±0.3	8.6±0.3	2139	23	-1.00	2164	38
14.2	0.000378	0.000011	0.281681	0.000022	1886	1.5±0.4	8.3±0.4	2148	29	-1.00	2179	48
15.1	0.000699	0.000021	0.281712	0.000020	1745	2.6±0.4	9.4±0.4	2107	27	-1.00	2111	44
16.1	0.000126	0.000005	0.281737	0.000019	1849	3.5±0.4	10.3±0.4	2073	25	-1.00	2055	41
Sample 07JG12 (t1 = 2500Ma, t2=1800Ma)												
2.1	0.000640	0.000024	0.281338	0.000031	2291	-10.7±0.6	5.3±0.6	2607	41	-1.00	2675	66
3.1	0.000624	0.000023	0.281473	0.000019	1796	-5.9±0.3	10.1±0.3	2426	25	-1.00	2380	41
4.1	0.005753	0.000231	0.281226	0.000042	2363	-14.9+0.7	1.0±0.7	2770	56	-0.99	2938	91
5.1	0.000333	0.000012	0.281434	0.000020	1786	-7.3±0.4	8.8±0.4	2478	27	-1.00	2464	45
8.1	0.000332	0.000012	0.281428	0.000020	1766	-7.5±0.4	8.5±0.4	2486	26	-1.00	2478	43
9.1	0.005874	0.000266	0.281510	0.000022	no	-4.9±0.4	11.0±0.4	2392	29	-0.99	2325	48
9.2	0.000648	0.000025	0.281347	0.000021	2187	-10.4±0.4	5.6±0.3	2595	28	-1.00	2656	46
12.1	0.000401	0.000014	0.281478	0.000027	1819	-5.7±0.5	10.3±0.4	2420	36	-1.00	2369	59
13.2	0.002150	0.000086	0.281294	0.000021	2221	-12.3±0.4	3.7±0.4	2669	29	-1.00	2776	47
14.1	0.003887	0.000167	0.281301	0.000027	1783	-12.2±0.5	3.8±0.4	2666	36	-0.99	2770	58
15.1	0.010489	0.000463	0.281499	0.000022	1786	-5.5±0.4	10.3±0.4	2419	30	-0.99	2370	49
Sample 07JG14 (t1 = 2500Ma, t2=1800Ma)												
3.1	0.029836	0.001108	0.281582	0.000025	1822	-3.4±0.5	12.1±0.5	2346	35	-0.97	2256	55
3.2	0.026136	0.000979	0.281555	0.000023	1717	-4.2±0.4	11.4±0.4	2376	31	-0.97	2302	50
4.1	0.006538	0.000263	0.281449	0.000024	1787	-7.0±0.5	8.9±0.5	2474	33	-0.99	2458	53
5.1	0.011601	0.000535	0.281351	0.000026	2563	-10.9±0.5	4.9±0.4	2624	35	-0.98	2700	56
5.2	0.013299	0.000517	0.281487	0.000034	387	-6.0±0.6	9.8±0.5	2439	46	-0.98	2402	74
6.1	0.008101	0.000298	0.281296	0.000022	1830	-12.5±0.4	3.4±0.4	2682	29	-1.0	2795	47
7.1	0.006782	0.000302	0.281504	0.000028	2400	-5.1±0.5	10.7±0.4	2403	38	-1.0	2343	62
8.1	0.004106	0.000163	0.281383	0.000022	1901	-9.3±0.4	6.7±0.4	2556	30	-1.0	2591	49
9.2	0.029982	0.001278	0.282075	0.000033	176	14.0±0.6	29.4±0.5	1670	46	-0.96	1190	72
10.1	0.005631	0.000210	0.281376	0.000023	1695	-9.6±0.4	6.3±0.4	2569	30	-0.99	2612	49
Sample 07JG30 (t=390Ma)												
No.	$^{176}Yb/^{177}Hf$	$^{176}Lu/^{177}Hf$	$^{176}Hf/^{177}Hf$	±(2σ)	Age (Ma)	$\varepsilon_{Hf(t)}$	±(2σ)	T_{DM1} (Ma)	±(2σ)	$f_{Lu/Hf}$		

1.1	0.029215	0.001231	0.282631	0.000029	393	3.3	0.5	886	42	-0.96
3.1	0.031191	0.001344	0.282678	0.000026	384	4.9	0.5	821	37	-0.96
5.1	0.041135	0.001808	0.282732	0.000035	397	6.7	0.6	754	50	-0.95
7.1	0.023913	0.001121	0.282702	0.000028	410	5.8	0.5	782	40	-0.97
8.1	0.036162	0.001620	0.282609	0.000029	389	2.4	0.5	926	42	-0.95
9.1	0.027403	0.001182	0.282710	0.000027	391	6.1	0.5	772	38	-0.96
10.1	0.033455	0.001502	0.282553	0.000044	425	0.5	0.8	1003	62	-0.95

Sample 07JG32 (t1 = 2100Ma, t2=1800Ma)

No.	$^{176}Yb/^{177}Hf$	$^{176}Lu/^{177}Hf$	$^{176}Hf/^{177}Hf$	±(2σ)	Age (Ma)	$\varepsilon_{Hf(t2)}$ ±(2σ)	$\varepsilon_{Hf(t1)}$ ±(2σ)	T_{DM1} (Ma)	±(2σ)	$f_{Lu/Hf}$	T_{DM2} (Ma)	±(2σ)
2.1	0.052867	0.002158	0.281424	0.000043	2082	-10.2±0.7	-3.9±0.8	2636	61	-0.94	2927	94
5.1	0.000469	0.000017	0.281523	0.000021	1908	-4.1±0.4	2.7±0.4	2359	28	-1.00	2523	45
6.1	0.000973	0.000036	0.281531	0.000030	1937	-3.9±0.5	3.0±0.6	2350	41	-1.00	2508	66
7.1	0.000270	0.000009	0.281495	0.000031	1778	-5.1±0.6	1.7±0.5	2396	42	-1.00	2584	68
9.1	0.000478	0.000018	0.281542	0.000031	1795	-3.5±0.5	3.4±0.5	2335	41	-1.00	2484	67
10.1	0.001333	0.000049	0.281505	0.000036	1761	-4.8±0.6	2.0±0.5	2386	49	-1.00	2567	79
12.1	0.026872	0.001162	0.281350	0.000038	2145	-11.7±0.7	2.0±0.6	2668	52	-0.97	3001	83
13.1	0.042025	0.001588	0.281486	0.000031	2124	-7.3±0.6	-0.8±0.5	2510	43	-0.95	2742	67
15.1	0.026188	0.001231	0.281421	0.000038	2093	-9.2±0.7	-2.6±0.7	2575	53	-0.96	2852	84
17.1	0.000632	0.000020	0.281523	0.000035	1690	-4.1±0.7	2.7±0.6	2360	46	-1.00	2524	76
18.1	0.003476	0.000163	0.281460	0.000033	2166	-6.6±0.6	0.3±0.5	2454	44	-1.00	2675	72
19.1	0.000516	0.000022	0.281554	0.000029	1941	-3.0±0.5	3.8±0.5	2319	38	-1.00	2457	62

Sample 07JG34 (t1 = 2500Ma, t2=1800Ma)

No.	$^{176}Yb/^{177}Hf$	$^{176}Lu/^{177}Hf$	$^{176}Hf/^{177}Hf$	±(2σ)	Age (Ma)	$\varepsilon_{Hf(t2)}$ ±(2σ)	$\varepsilon_{Hf(t1)}$ ±(2σ)	T_{DM1} (Ma)	±(2σ)	$f_{Lu/Hf}$	T_{DM2} (Ma)	±(2σ)
1.1	0.006343	0.000234	0.281261	0.000021	2458	-13.7±0.4	2.2±0.4	2724	28	-0.99	2864	45
3.1	0.012047	0.000446	0.281328	0.000019	2485	-11.6±0.4	4.2±0.4	2649	26	-0.99	2740	42
4.1	0.006986	0.000263	0.281326	0.000022	2203	-11.4±0.4	4.5±0.4	2640	29	-0.99	2727	47
5.1	0.008959	0.000333	0.281288	0.000018	2567	-12.8±0.3	3.0±0.3	2695	25	-0.99	2815	40
7.1	0.004794	0.000180	0.281332	0.000021	2389	-11.1±0.4	4.8±0.4	2626	28	-0.99	2704	45
11.1	0.007860	0.000297	0.281321	0.000019	2540	-11.7±0.4	4.2±0.4	2649	26	-0.99	2741	42
12.1	0.003820	0.000146	0.281282	0.000019	2466	-12.8±0.4	3.1±0.3	2690	25	-1.00	2808	41
14.1	0.005750	0.000223	0.281330	0.000024	2683	-11.2±0.5	4.7±0.5	2631	33	-0.99	2713	53
15.1	0.049588	0.001917	0.281391	0.000023	2287	-11.1±0.4	4.0±0.4	2665	32	-0.94	2756	50
17.1	0.024919	0.000946	0.281368	0.000018	2161	-10.7±0.3	4.8±0.3	2628	25	-0.97	2704	39
18.1	0.004660	0.000206	0.281234	0.000018	2403	-14.60.4±	1.3±0.3	2758	25	-0.99	2919	40
19.2	0.014326	0.000637	0.281290	0.000025	2148	-13.1±0.5	2.6±0.5	2713	34	-0.98	2842	55
20.1	0.005367	0.000214	0.281312	0.000027	2759	-11.9±0.5	4.1±0.5	2655	36	-0.99	2752	58
22.1	0.006858	0.000275	0.281317	0.000019	2147	-11.8±0.4	4.0±0.4	2653	26	-0.99	2747	42

Figure 1

Click here to download high resolution image

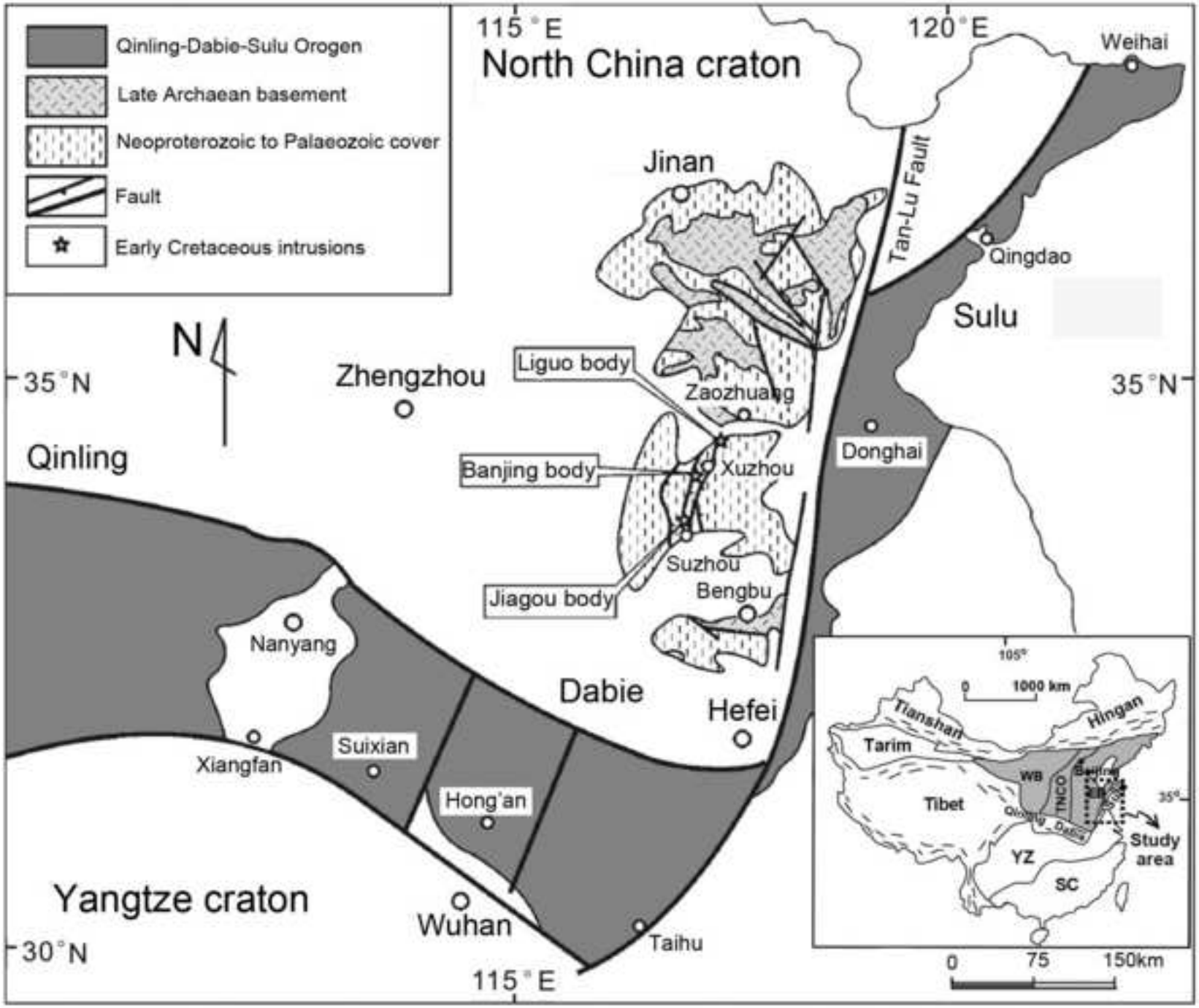

Figure 2

Click here to download high resolution image

Figure 3

Click here to download high resolution image

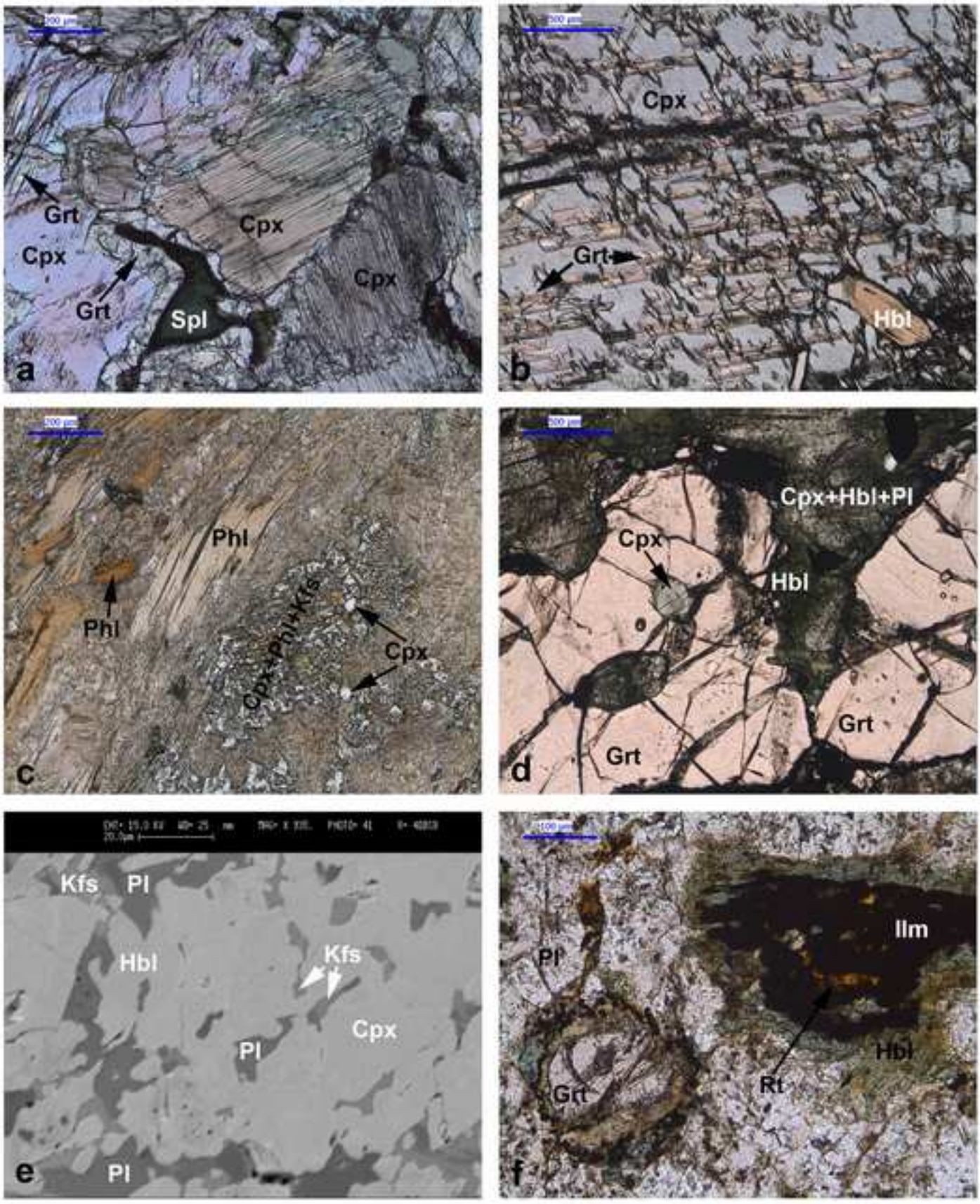

Figure 4

Click here to download high resolution image

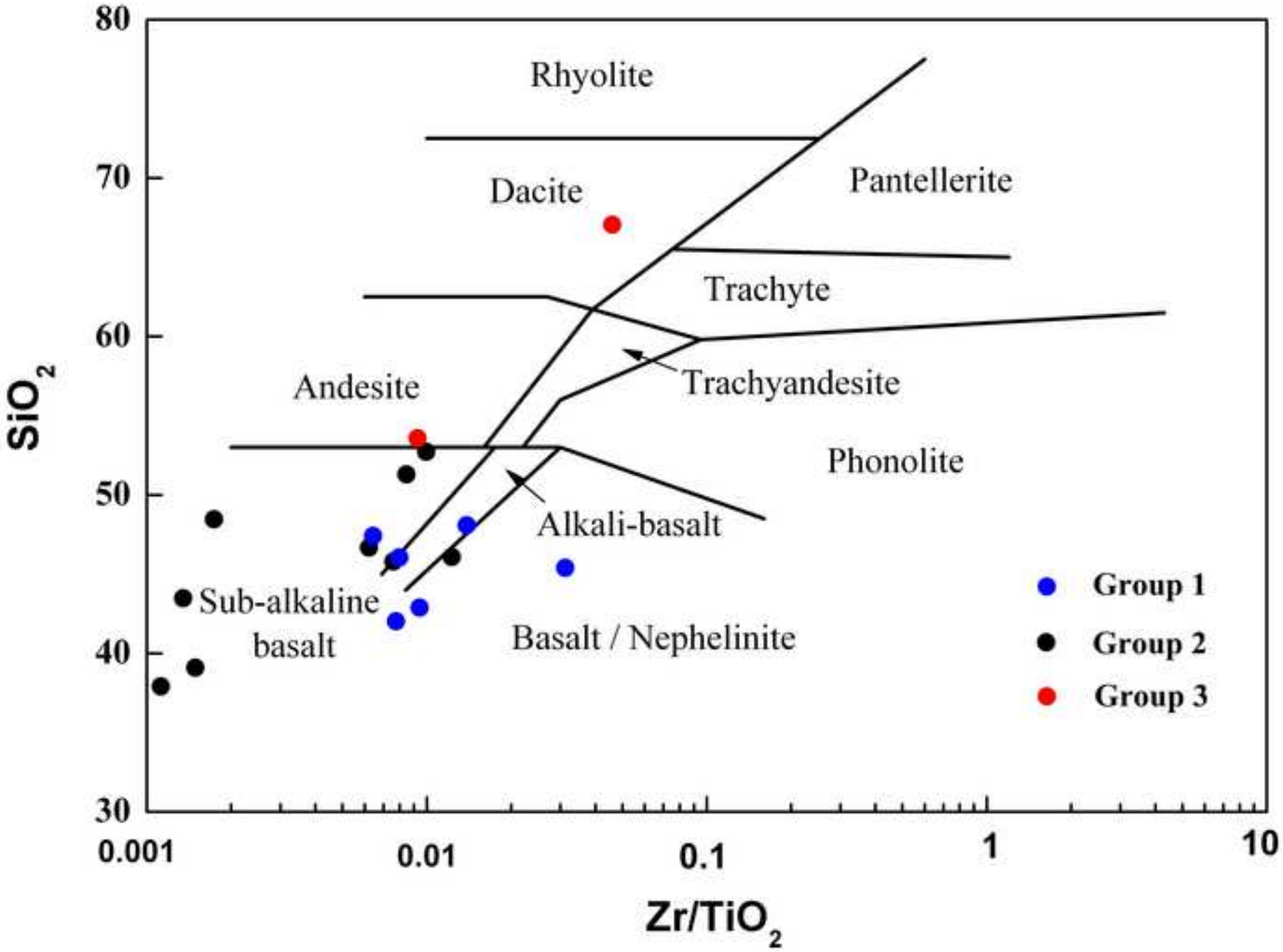

Figure 5

Click here to download high resolution image

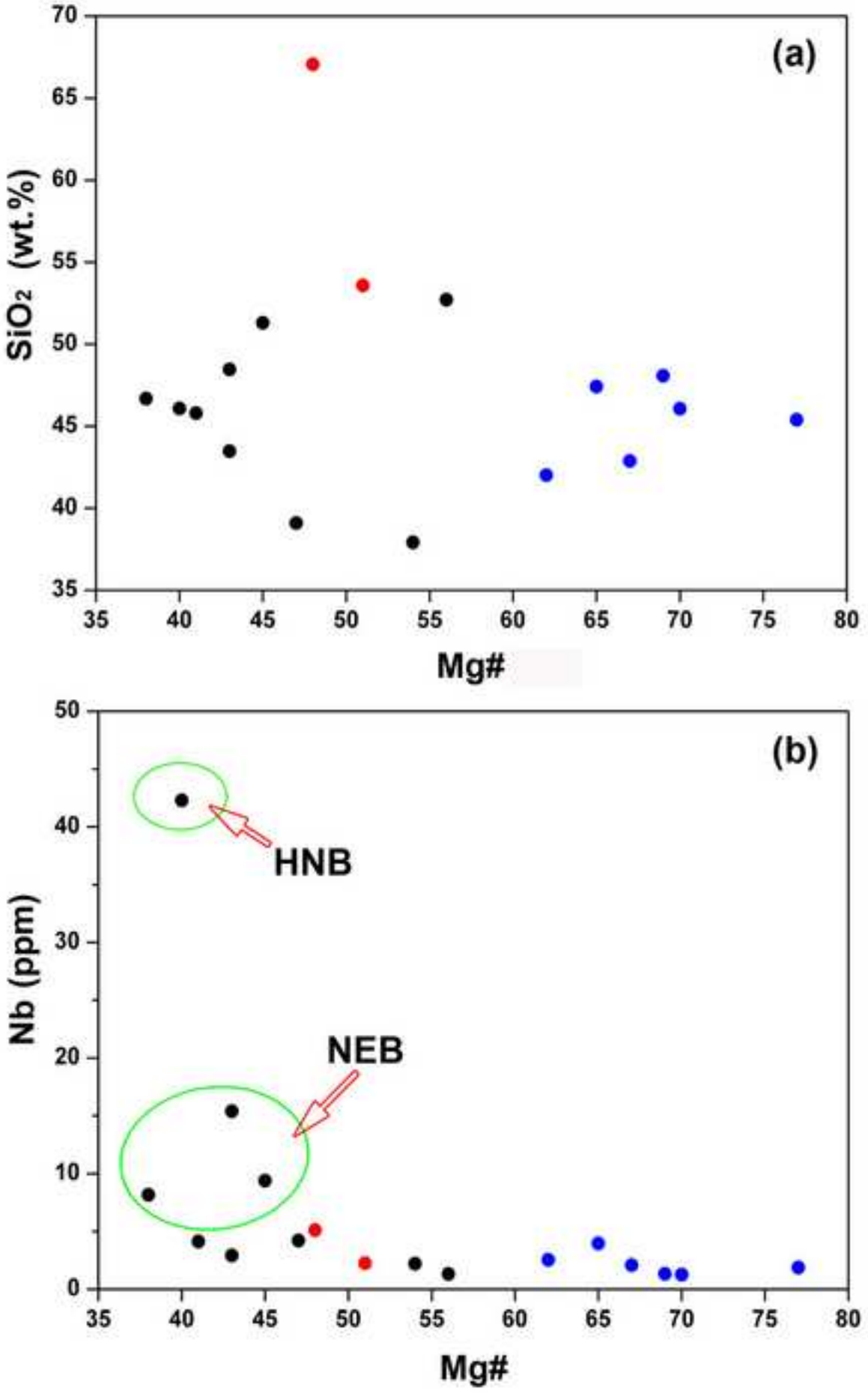

Figure 6

Click here to download high resolution image

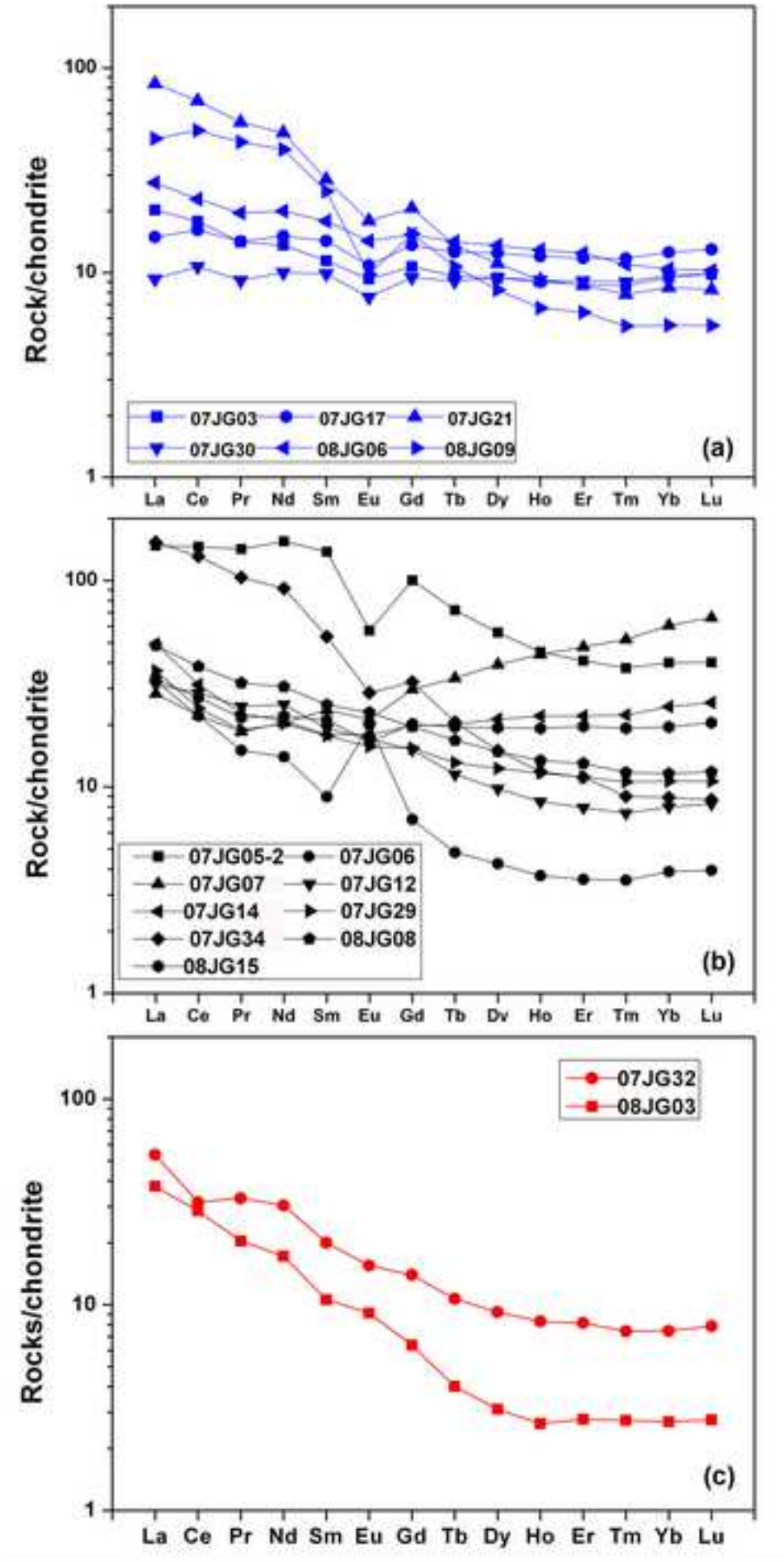

Figure 7

Click here to download high resolution image

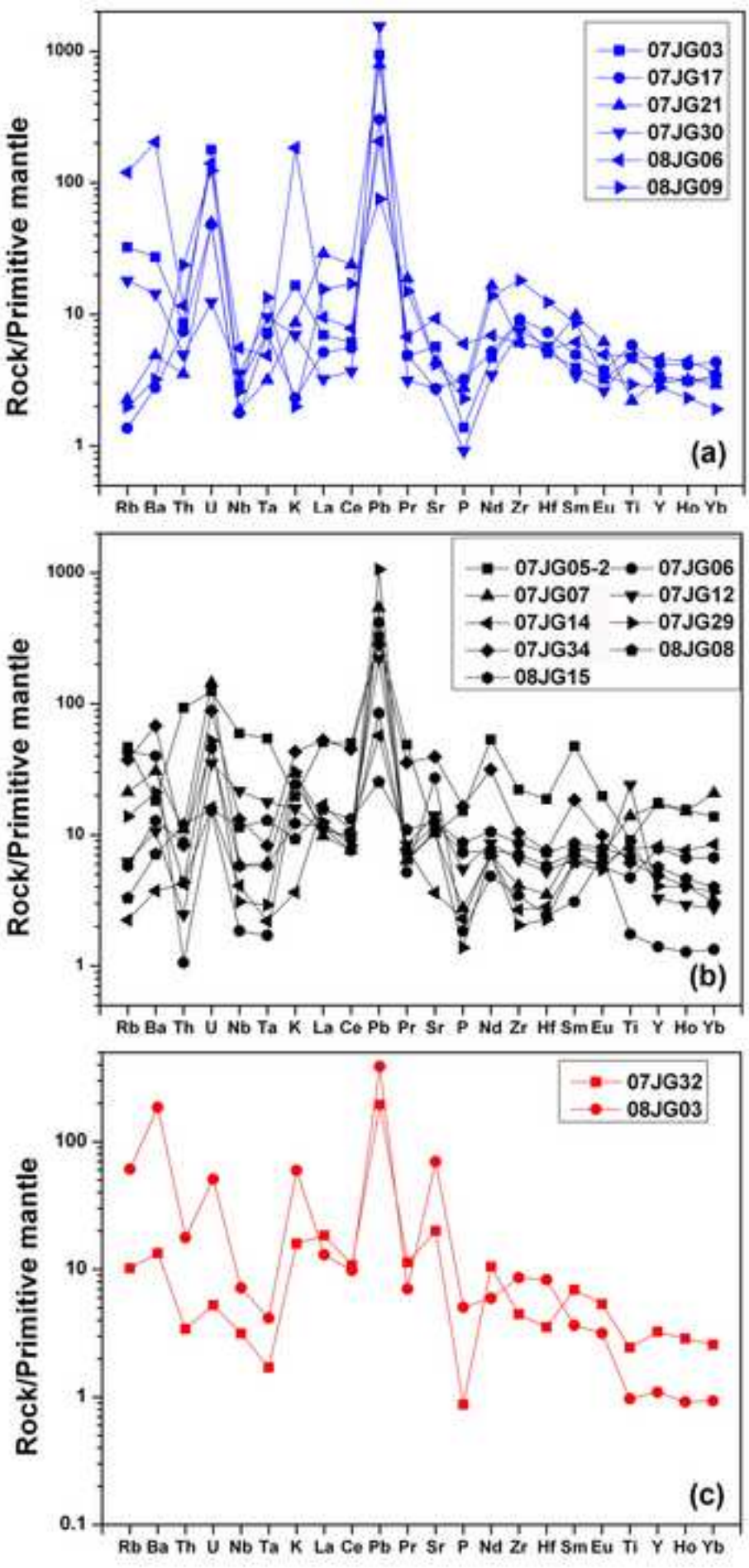

Figure 8

Click here to download high resolution image

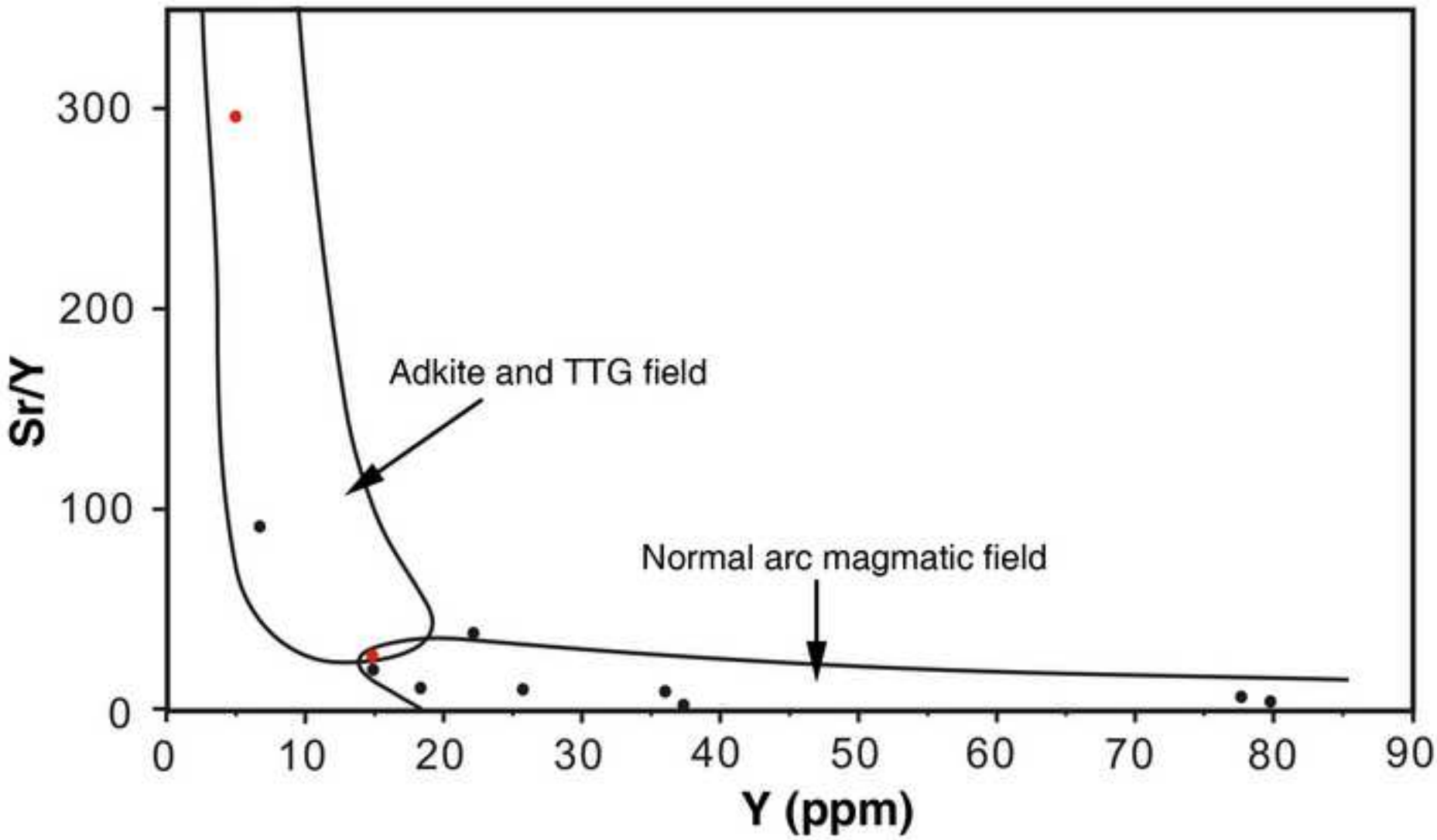

Figure 9

Click here to download high resolution image

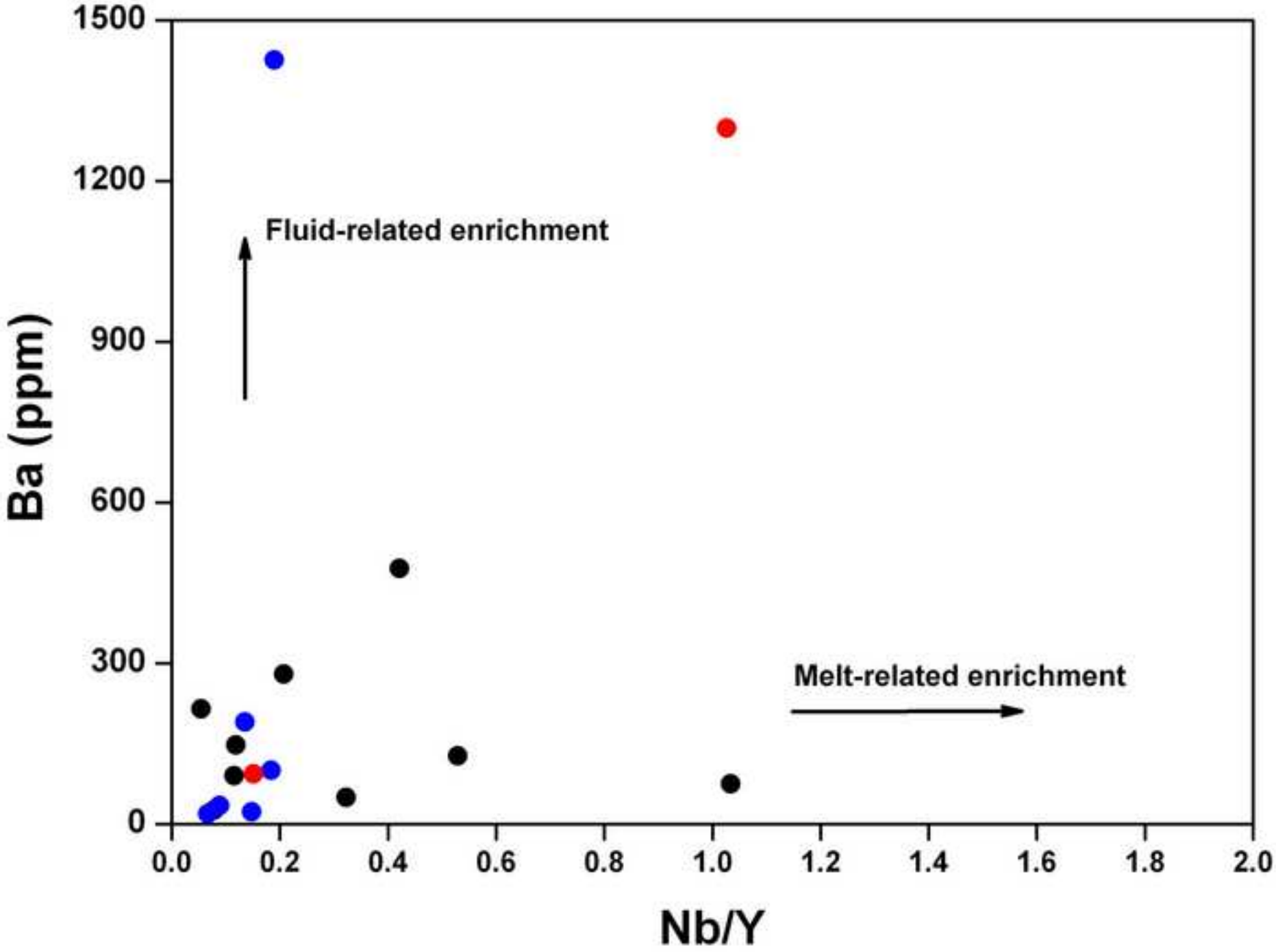

Figure 10

Click here to download high resolution image

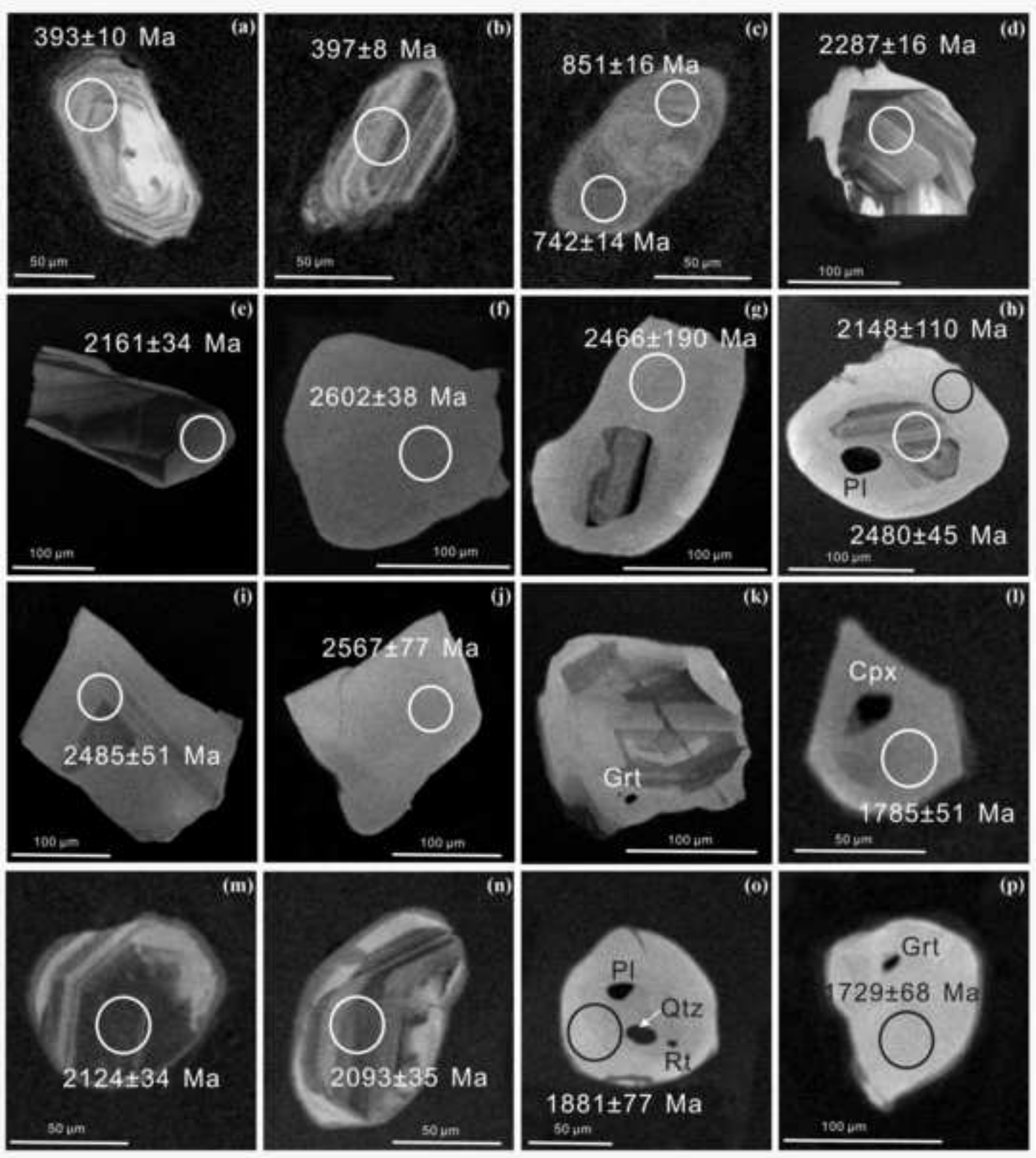

Figure 11

Click here to download high resolution image

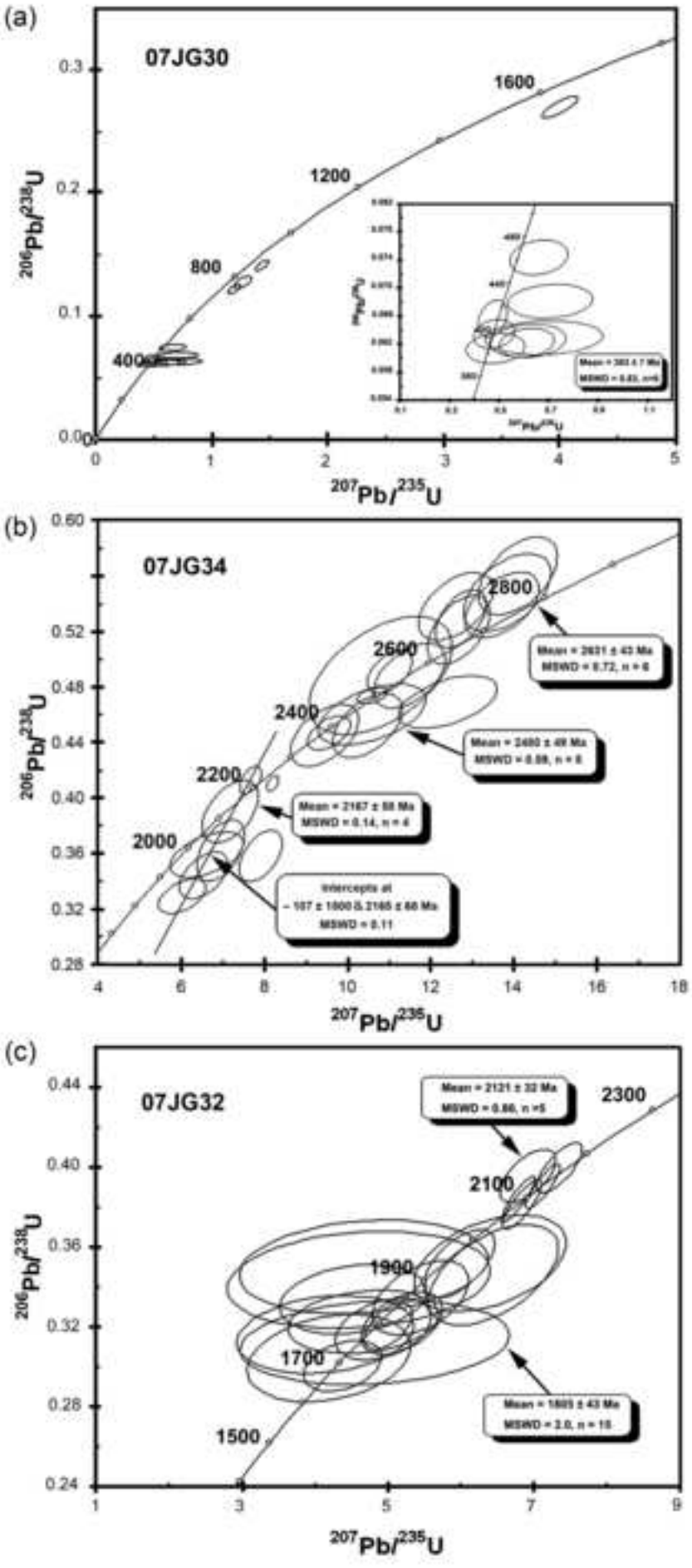

Figure 12

Click here to download high resolution image

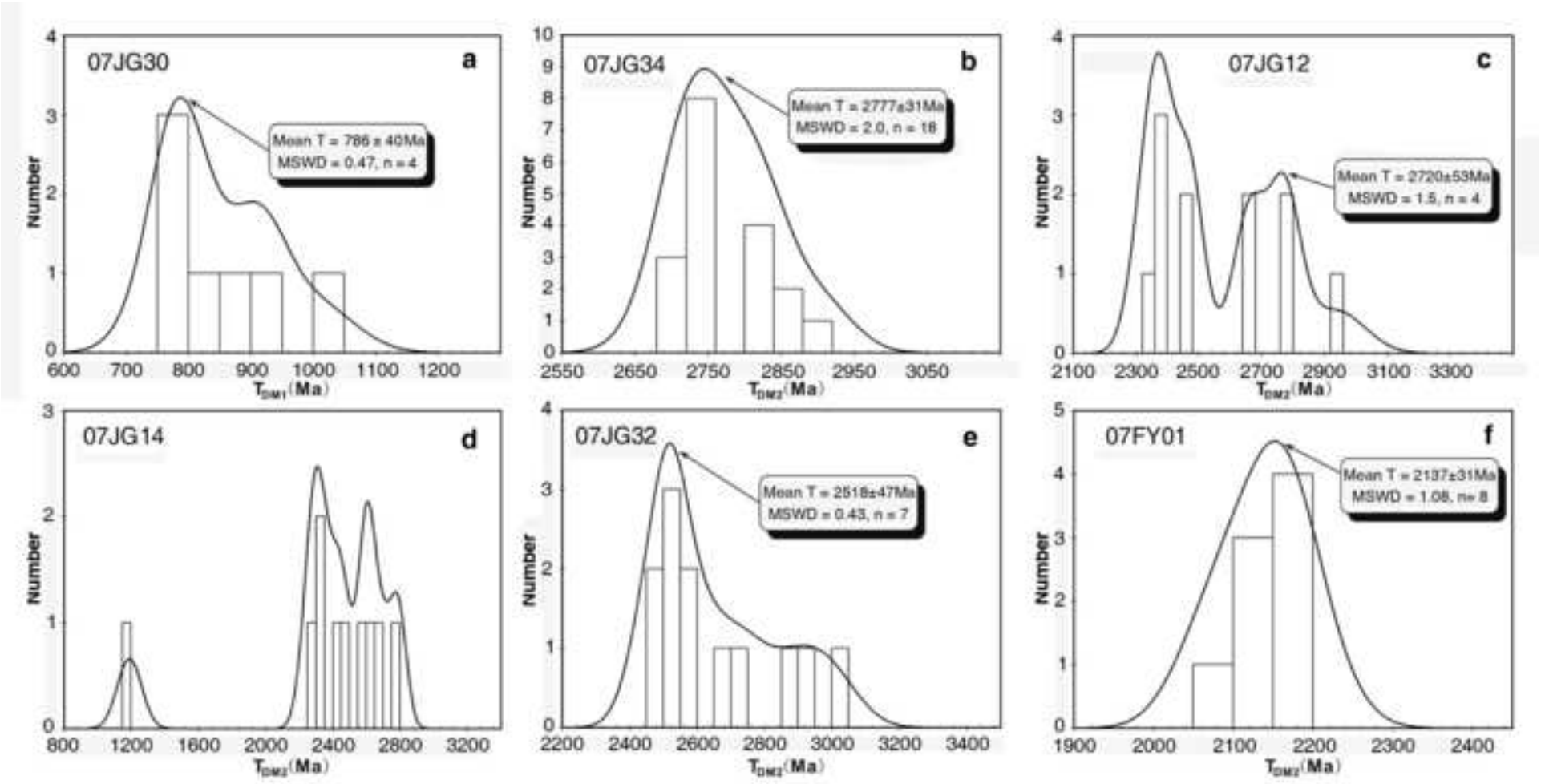

Figure 13

Click here to download high resolution image